ASTRONOMY & ASTROPHYSICS
SUPPLEMENT SERIES

Astron. Astrophys. Suppl. Ser. **55**, 143-161(1984)

Revision of solar equivalent widths, Fe I oscillator strengths and the solar iron abundance

R. J. Rutten and E. B. J. van der Zalm

Sterrewacht « Sonnenborgh », Zonnenburg 2, 3512 NL Utrecht, The Netherlands

Received July 4, accepted October 12, 1983

Summary. — We employ detailed modelling of solar Fe I and Fe II lines to calibrate the correction of equivalent widths for contamination by unresolved blends. We then determine the equivalent widths of 750 clean lines in the Jungfraujoch Atlas of the optical solar spectrum, and we compare these to the values given for the Utrecht Atlas by Moore *et al.* (1966). We also select clean Fe I lines, discuss their NLTE formation, construct a NLTE Fe I curve of growth, provide new oscillator strengths for weak Fe I lines, and revise the solar iron abundance to $N_{Fe}/N_H = (4.3 \pm 0.5)\ 10^{-5}$.
We use the results to appraise the basis and methods of classical stellar abundance determination.

Key words : stellar photospheres — solar spectral lines — curve of growth — transition probabilities — iron abundance.

1. Introduction.

This paper completes a series of three in which the optical solar Fe I spectrum is scrutinized to assess conventions of classical stellar abundance analysis. After discussing Fe I oscillator strengths, the NLTE formation of Fe I lines and the Fe I curve of growth in the preceding papers (Rutten and Kostik, 1982, henceforth paper RK; Rutten and Zwaan, 1983, henceforth paper RZ), we turn now to the observational input of classical abundance determination : to the *equivalent widths*.

The standard reference for equivalent widths of optical solar lines is the compilation by Moore, Minnaert and Houtgast (1966, henceforth MMH) [1], which is based on the 40-year old Utrecht Atlas (Minnaert *et al.*, 1940). Here, we use the much more precise Jungfraujoch Atlas (Delbouille *et al.*, 1973) to furnish a consumer report on the quality of the MMH values. Such an appraisal is of interest to stellar studies because stellar techniques now permit a similar advance : while the Utrecht Atlas finds its stellar counterpart in conventional high-dispersion photographic Coudé spectrography, most notably in the Griffin Atlases (Griffin, 1968; Griffin and Griffin, 1979), the photoelectric double-pass Jungfraujoch Atlas sets an example of spectral purity now in reach of stellar instruments, most notably the ESO Coudé Echelle Spectrometer (Enard, 1981). This advance is important because spectral resolution is the prime domain of resolution in which stellar phenomena can be studied with solar-like sophistication (see Rutten and Cram, 1981). It therefore behooves solar spectroscopy to ascertain what precision is required for which sophistication; we do this here for abundance determination, with Fe I as archetypical example.

In paper RZ, it was found that the oscillator strengths of weak Fe I lines are now so well determined (Gurtovenko and Kostik, 1981) that equivalent widths have replaced the oscillator strengths as major error source, implying that revision of the MMH values promises worthwhile improvements not lost in other noise. However, we find revision of the equivalent width of all 5000 solar Fe I lines (or, *a fortiori*, of all 24000 MMH lines) too large an undertaking even in the computer era, because it requires blend removal through detailed profile synthesis for most lines. We rather discuss here only *clean* weak lines, without discernable blends. Fortunately, there are enough of these present to permit evaluation of the MMH values, and of the Fe I curve of growth.

Even clean lines are often contaminated by unresolved blends; in the violet, these constitute together an appreciable quasi-continuous « line haze ». We derive appropriate corrections in section 2 on the basis of published NLTE modelling of solar Fe I and Fe II lines. We also address the old but unavoidable problem of locating the « true » continuum. In section 3 we select all clean weak lines from the Jungfraujoch Atlas and compare their equivalent widths with the MMH values. In section 4 we select the clean Fe I lines and discuss their curve of growth.

With this paper, on solar equivalent widths and the curve of growth, ends a Utrecht tradition which started

[1] We thank J. W. Harvey at Kitt Peak National Observatory for a listing of MMH on computer tape. Copies can be obtained from E.v.d.Z.

Send offprint requests to : R. J. Rutten.

50 years ago when Minnaert and coworkers introduced these concepts, and which culminated in the Utrecht Atlas and the MMH compilation. Coauthor to both was J. Houtgast, who died at Utrecht on 1 november, 1982. We dedicate this paper to his memory.

2. Reduction.

2.1 CORRECTIONS FOR UNRESOLVED BLENDS. — Many spectral lines do not reach the « true » continuum I_c^T set by the free-free processes, the bound-free processes and the continuum-scattering processes. Instead, they are blended by unresolved weak lines and/or the overlapping wings of nearby strong lines, which effectively combine into an extra quasi-continuous process and modify the observed background intensity to a lower « local » continuum I_c^L (Fig. 1).

In this section we employ model computations to study how this change in background affects equivalent widths. We assume at first that the change indeed mimics the true continuum in formation, i.e. that the extra contribution by the unresolved blends to the total opacity is constant over the line width, and that it has the same height-dependence as the true continuous opacity.

We model the difference between the « true » equivalent width W^T, which we define as the equivalent width which a line would have in the absence of this additional quasi-continuous opacity (Fig. 1), and the actually measured « local » equivalent width W^L by comparing iron lines computed with and without enhancements of the continuous opacity. We have used the computer program and the standard setup of paper RZ, adopting the same atmospheric model, turbulence, partition functions, damping formalisms, etc. We again use the height-dependent NLTE departure coefficients for the Fe I a^3 F and z^5 G° levels from Lites and White (1973), and the coefficients for the Fe II a^6 D and z^7 D° levels from Cram *et al.* (1980). These sets are representative for most Fe I and Fe II lines, respectively; they are shown and discussed in paper RK. We enter the opacity enhancements by height-independent multiplication factors $1 + \varepsilon$ to the combined continuous opacities from H, H^- and the metals; the scattering processes (Thomson and Rayleigh) are not changed.

We have computed the equivalent widths of many such representative Fe I and Fe II lines, varying the opacity increment ε, the oscillator strength *gf*, the lower-level excitation energy χ and the wavelength λ. Figure 2 shows results covering the range of these variables in realistic combinations; the computed continuum ratios I_c^L/I_c^T are specified in table I.

The line-strength corrections $\log(W^T/\lambda) - \log(W^L/\lambda)$ in figure 2 vary from quite small for short wavelengths and low excitation, to appreciable for long wavelengths and high excitation; they are larger for Fe II than for Fe I. For example, the $\varepsilon = 10\,\%$ curve for Fe I lines at $\lambda = 400$ nm, $\chi = 1$ eV (upper solid curve in the lefthand panel) does not reach the 3 % difference level, while the $\varepsilon = 5\,\%$ curve for Fe II lines at $\lambda = 800$ nm, $\chi = 4.5$ eV reaches the 5 % difference level for very weak lines (upper dashed curve in the righthand panel). Except for the latter lines, all corrections are *smaller* than the adopted opacity increments ε. The computed continuum decrements $1 - I_c^L/I_c^T$ are also smaller than ε (Table I).

For a given observed line strength $\log(W^L/\lambda)$ and opacity increment ε, the line-strength corrections increase with the excitation energy and with the wavelength. Since the corresponding continuum ratios I_c^L/I_c^T increase with wavelength, the corrections increase also with wavelength for a given continuum ratio.

Figure 2 shows further that the correction curves reflect the slope of the curve of growth. They are constant for the weakest lines, and then dip to a minimum which is located at the onset of the flat part of the curve of growth, and which shifts leftward for increasing wavelength in accordance with the flat part's wavelength forking. For stronger lines the curves rise again until they flatten out at right, with a slight decrease for the Fe II lines.

We explain these various features by refering to the classical derivation of the curve of growth assuming a Milne-Eddington atmosphere, LTE, linear variation of the Planck function with the optical depth τ, and a single, characteristic layer of line formation. We then have (e.g. Mihalas, 1970, Eq. 11-51):

$$W = 2\,\frac{\mathrm{d}B/\mathrm{d}\tau}{B_0 + \mathrm{d}B/\mathrm{d}\tau}\,\Delta\nu_D \int_0^\infty \frac{\eta}{1+\eta}\,\mathrm{d}\nu$$

where B_0 is the surface value of the Planck function, $\Delta\nu_D$ is the height-independent Dopplerwidth, $\eta = l(\nu)/k_c$ is the ratio of the line absorption coefficient to the continuous absorption coefficient, and ν is the frequency. For weak lines this results in (Mihalas 1970, Eq. 11-53):

$$W^T (:)\ \eta_0\,\Delta\nu_D\,\frac{\mathrm{d}B}{\mathrm{d}\tau}$$

where η_0 is the line-center opacity ratio l_0/k_c. Our multiplication of the continuous absorption coefficient k_c by $1 + \varepsilon$ leads to:

$$W^L (:)\ \frac{\eta_0}{1+\varepsilon}\,\Delta\nu_D\,\frac{\mathrm{d}B}{(1+\varepsilon)\,\mathrm{d}\tau} \approx \frac{W^T}{1 + 2\,\varepsilon}.$$

Similarly, we find $W^L (:)\ W^T/(1+\varepsilon)$ for lines from the flat part of the curve of growth, and $W^L (:)\ W^T/(1 + 1.5\,\varepsilon)$ for lines from the damping part. Thus, the predicted line-strength correction curves start at twice the enhancement ε, drop to a minimum equal to ε, and rise again to a value of $1.5\,\varepsilon$, independent of wavelength and excitation energy.

The actual correction curves in figure 2 follow this pattern but at much smaller values, and they vary with the wavelength and the excitation energy. These discrepancies result from the differences between the real sun and the simplifying assumptions above. The enhancement ε causes a slight increase in the mean height of formation, amounting to a few km for $\varepsilon = 10\,\%$. While the actual Dopplerwidth and the actual gradient of the source function are but slightly smaller at the larger height, there is an appreciable increase in η_0, reaching up to 20 %. This increase largely cancels the corrections derived above, and its variation with the wavelength and the excitation energy sets the differences between the curves of figure 2.

We show the behaviour of η_0 for iron lines in the photosphere in figure 3. For all types of iron line there is a steep increase with height in the low photosphere because the line opacity scales with the hydrogen density while the continuous opacity, largely due to bound-free H^- transitions, scales with the product of the hydrogen and electron densities. The Fe II curves in figure 3 flatten out at larger heights because of the sensitivity of the Boltzmann population factor to the decreasing temperature; its effect is strongest for high-excitation lines. The Fe I curves remain steeper at first because the fraction of neutral iron atoms increases by a factor of 5 between $h = 0$ and $h = 300$ km, in contrast to the ion fraction which decreases by 13 %. Above $h = 200$ km the onset of NLTE overionization produces underpopulation of the lower levels of the Fe I lines and flattens the Fe I curves, in contrast to the Fe II lines of which the lower levels have LTE populations at all heights.

The curves in figure 3 are nearly identical for different wavelengths because both $l_0(h)$ and $k_c(h)$ happen to increase linearly with the wavelength throughout the visual. However, the mean height of continuum formation increases by about 40 km between $\lambda = 400$ nm and $\lambda = 800$ nm (arrows); at longer wavelengths a less steep gradient of η_0 is sampled, resulting in larger line-strength corrections.

The behaviour of η_0 and the values of the line-strength corrections for other spectra than Fe I and Fe II will generally be very similar, so that our results hold for most lines. Significant departures will occur only if the height-dependence of the ionization balance differs strongly in the deep photosphere; for example, if the fraction of neutral atoms increases less rapidly outwards than the neutral iron fraction, the neutral-atom corrections will be closer to the Fe II corrections. This will be the case for atoms of large ionization energy.

Finally, we abandon our assumption that the continuous opacity enhancement ε is height-independent, i.e. that the unresolved blends behave as the true continuum in their formation. If we assume instead that the blends are all Fe I lines, we have to replace the opacity factor $1 + \varepsilon$ by $1 + \alpha \eta_b$, with η_b the height-dependent line-center opacity ratio of a typical Fe I blend. We have done this for various combinations of Fe I lines and Fe I blends. In each case we have adjusted the constant α so that the computed continuum ratio I_c^L/I_c^T equals the corresponding $\varepsilon = 5$ % value in table I, to enable direct comparison with the 5 % curves of figure 2. We find that for all combinations the line-strength corrections $\log (W^T/\lambda) - \log (W^L/\lambda)$ are *smaller* than in figure 2. The cause of this reduction is that the slower outward decrease of the effective continuous absorption coefficient implies that the same continuum ratio is reached already for a relatively small value of α.

The reductions are largest for weak high-excitation Fe I lines with low-excitation Fe I blends in the violet, where they reach 50 % of the corrections (which are already small for such lines). The reductions are smallest for weak low-excitation Fe I lines with high-excitation Fe I blends in the red, amounting to 10 %. For more realistic combinations the reductions are typically 20 % for weak lines; they are smaller for stronger lines and for Fe II lines.

We conclude from these tests that the curves of figure 2 represent slight overestimations due to our choice of a height-independent factor $1 + \varepsilon$, which we nevertheless maintain because we would need detailed specification of the blends otherwise. We have computed curves for Fe I lines as those in figure 2 for a grid of 5 wavelengths, 5 excitation energies and 7 opacity enhancements, at considerable computational expense because the implied double subtraction of nearly equal numbers requires large precision, thus finely spaced integration grids. To permit usage of these results without having to interpolate in extensive 4-parameter tables, we approximate all combined Fe I results by the adequate functional representation given in table II. It was derived with a general least-squares function-fitting program following Powell and Macdonald (1972). The tests above show that reduction by 20 % is a reasonable correction for the neglect of the height-dependence of the blends, and figure 2 shows that increase by 40 % represents a reasonable approximation to the Fe II corrections.

Note that for weak lines the equivalent-width corrections represent line-depth corrections as well, and that the smallness of the corrections implies that measurements directly from the true continuum would have very large errors for very weak lines. For example, measuring lines of 1 % depth and 99 % continuum ratio from the true continuum would be in error by 0.3 dex, whereas measurement from the local continuum without further correction would be in error by less than 0.004 dex. Thus, it is much more important to locate the local continuum precisely than to locate the true continuum precisely (which is fortunate for segmented recording, as with a cross-dispersed échelle spectrometer).

We summarize this section in the form of a recipe. If there is a difference between the true and the local background, the worst one can do is to measure equivalent widths and line depths directly from the true continuum (e.g., Elste, 1978). Measurement from the *local* continuum, however, produces quite good approximations because the corrections derived above are very small, especially for lines in the blue, at low excitation, and from a neutral atom. Application of table II to correct these measurements increases the precision. Further improvement requires detailed spectral synthesis of the unresolved blends as well as the line.

2.2 THE TRUE CONTINUUM. — We use the magnetic-tape edition of the Jungfraujoch Atlas which extends from $\lambda = 400.6$ nm to $\lambda = 800$ nm. The Atlas specifies the solar disk-center intensity at 0.2 pm intervals in arbitrary units. A compressed plot of the whole Atlas is shown in figure 4. The upward spikes in the top panel of each wavelength strip mark the continuum windows on an exaggerated vertical scale. The thick solid line in the top panels is the estimate for the true continuum specified by Ardeberg and Virdefors (1975, 1979). It is the result of their least-square piece-wise linear fits to the Atlas intensities in 83 continuum windows which are free of discernable lines, and supposedly reach the true continuum. Their determination ends at $\lambda = 686$ nm; we have extended it here to $\lambda = 800$ nm in the same spirit, although by eye rather than per computer. Table III specifies the junction points of the complete polygon.

Ardeberg and Virdefors assume that their continuum windows sample the possible variations of the true continuum and of the instrumental response well enough.

However, this is not the case because the window separations often exceed the lengths of the original Atlas data segments, which were each straightened, connected to the adjacent segments, and normalized in somewhat arbitrary manner by Delbouille *et al.* The problem of how to patch short segments together is inherent to the use of a spectrum-scanning spectrometer; it vanishes when a broad-band Fourier Transform spectrometer is used. In figure 5 we compare the Jungfraujoch Atlas to data taken with the Kitt Peak FTS in the setup described by Brault (1978, example 2), for the region of overlap. The FTS data are shown reversedly on top; each of the two data sets was normalized to a straight line (dotted) through the two marked peaks. The true continuum is not known, but for this short wavelength range it should be nearly linear. Irrespective of the location and the tilt of the true continuum, figure 5 should be symmetrical with respect to the two dotted lines. It is not; there are deviations over 1 %. Since the FTS continuum is straight, these are due to the varying tilts of the individual Atlas segments, of which the junctions are indicated. The true Atlas continuum will therefore be a polygon of segments with lengths of about 1 nm, varying much more rapidly than the extended Ardeberg-Virdefors continuum of figure 4 and table III.

Another issue is whether the windows employed are indeed fully free from lines. Ardeberg and Virdefors (1979) warn that the good consistency of their fit in the violet does not guarantee that it represents the truly continuous background, although they then proceed to use it as such; here, we assume that it severely underestimates the line haze in the violet, notwithstanding the high spectral resolution of the Jungfraujoch Atlas. We base this view on the studies by Holweger (1970) and by Vernazza, Avrett and Loeser (1976). In particular, figure 26 of the latter paper shows a « $k = 2$ » model, based on the theoretical line-opacity distribution functions of Kurucz, Peytremann and Avrett (1974), which fits the peak intensities of Labs and Neckel (1970) well. Figure 3 of the same paper indicates that the corresponding line-haze opacity amounts to 10 % of the line-free continuous opacity near $\lambda = 400$ nm and to 1 % near $\lambda = 500$ nm at the height of continuum formation. The corresponding intensity reductions, respectively 7 % and 0.6 %, are smaller than Holweger's (1970) estimate from older data, but they agree well enough and they are large enough that they should not be ignored.

We summarize this section in the form of a desideratum. While the Jungfraujoch Atlas represents a major improvement over the Utrecht Atlas, the ultimate solar intensity atlas has yet to appear. It should not only be of high spectral purity, but also solve the segmentation problem by broad-band measurement and the line-haze problem by having an absolute intensity scale, enabling direct comparison to computed models. Obviously, the Kitt Peak FTS is the prime instrument to achieve this goal.

3. The clean lines.

3.1 LINE SELECTION. — We have scanned the Jungfraujoch Atlas for clean lines with a computer program which detects spectral lines, rejects them if they fail various cleanliness criteria, modifies them if slight blends appear present, and measures various profile parameters.

The smoothness of the Atlas data permits detection of a spectral line simply by defining a line as the Atlas segment between two successive maxima I_c^1 and I_c^2 (Fig. 1). We reject lines in the following cases :

(*a*) if one or both of the maxima has $d > 0.03$ where $d = (I_c^{AV} - I_\lambda)/I_c^{AV}$ measures the fractional depth from the extended Ardeberg-Virdefors continuum in table III;

(*b*) if the two maxima differ more than 0.01 in d;

(*c*) if the lowest of the two maxima has $d > 0.5\ D$, with D the value of d at the minimum;

(*d*) if $\log (W/\lambda) < -7$;

(*e*) if the wavelength shift between the normalized first moments of the whole profile and of the lower part with $d \geqslant 0.7\ D$ exceeds 1.0 $\lambda/500$ pm;

(*f*) if the wavelength shift between the location of the minimum and the normalized first moment of the lower part exceeds 0.25 $\lambda/500$ pm.

We so reject all lines with resolved blends (criteria *a-c*), and all lines with unresolved blends that cause noticeable deformations (criteria *e* and *f*). This automatically ensures selection of weaker lines only, because there are no lines stronger than $\log (W/\lambda) = -4.6$ without blends.

For the line identifications we accept the entries in MMH. We reject the line if there is no entry in MMH within 3 pm of the line-center wavelength, or if there are multiple entries; we also reject the line if it is identified as telluric or molecular, if there is no excitation energy given, or if the line is marked as blended.

Inspection shows that the majority of the lines so selected still has small asymmetries, mostly in the wings. While some asymmetry should be present due to convection (see Dravins *et al.*, 1981), much of it is often clearly due to a nearby line affecting one wing. We have therefore used only the half of the profile with the highest maximum of all lines for which the two maxima differ by more than 0.003 in d, or for which the wavelength shift between the first moments of the whole profile and of the lower part differs by more than 0.25 $\lambda/500$ pm.

Finally, we have divided the measured area of each line by the area of a gaussian profile with the same halfwidth and plotted the ratio against the line strength (plot not shown). Lines with an unresolved blend in their core have too small a ratio compared to the average trend, while lines with an unresolved blend in a wing have too large a ratio. We have deleted all lines outside the 90 % confidence limits of a least-square fit.

In table IV we specify the results for the remaining lines, of which there happen to be precisely 750. The line wavelength (first column) is the value of the normalized first moment of the lower part of the profile in Atlas units. The identification (spectrum and multiplet number) is from MMH. The parameter « mode » is W for the 154 really clean lines of which the whole profile was used, B if only the blue half and R if only the red half was used. The line depth D^L is measured from the local continuum I_c^L, defined at the intensity of the highest of the two maxima (Fig. 1). The halfwidth at half maximum FWHM is measured in pm at 0.5 D^L. The local line strength $\log (W^L/\lambda)$ was found by applying trapezoidal integration to the Atlas profile between the two maxima, or between the minimum and the highest maximum for the halved lines; the latter values were doubled.

To obtain the true line strengths $\log(W^{\mathrm{T}}/\lambda)$ in the last column we have applied background corrections following section 2. By defining $I_{\mathrm{c}}^{\mathrm{L}}$ at the highest adjacent maximum, we assume that the Jungfraujoch Atlas fully resolves the background windows as they are present in the incident solar spectrum. We further assume that the extended Ardeberg-Virdefors continuum $I_{\mathrm{c}}^{\mathrm{AV}}$ represents the true continuum $I_{\mathrm{c}}^{\mathrm{T}}$ in Atlas units above $\lambda = 550$ nm, but underestimates it by 0.6 % at $\lambda = 500$ nm and by 7 % at $\lambda = 400$ nm, respectively; we have interpolated these line-haze deficits by cubic spline for intermediate wavelengths. We also assume that the resulting ratio $I_{\mathrm{c}}^{\mathrm{L}}/I_{\mathrm{c}}^{\mathrm{T}}$, specified in the next-to-last column, is constant over the line profile; this is a fair assumption in view of our line-selection and line-halving criteria. The corrections were found by entering the continuum ratio $I_{\mathrm{c}}^{\mathrm{L}}/I_{\mathrm{c}}^{\mathrm{T}}$, the local line strength, the wavelength and the excitation energy (from MMH) in the approximation of table II. The result was decreased by 20 % for all lines, and increased again by 40 % for all ion lines. Thus, we have corrected all lines as if they were iron lines of the corresponding ionization stage, and blended by typical Fe I blends.

The number of lines per spectral species is specified in table V. Iron supplies half of the total, demonstrating that, with so many lines free from blends and free from hyperfine structure, iron is the prime provider of optical diagnostics. Note, however, that MMH count 2300 unblended Fe I lines between $\lambda = 400$ nm and $\lambda = 800$ nm. Only a minor fraction is here qualified « clean », and most of these are yet slightly blended.

3.2 Equivalent widths. — We compare the equivalent widths of the 750 clean lines and their corrections with those of MMH in figure 6, against line strength (left) and wavelength (right). We first discuss the top panels. They show our corrections $\Delta_{\mathrm{JJ}} \equiv \log(W_{\mathrm{JJ}}^{\mathrm{T}}/\lambda) - \log(W_{\mathrm{JJ}}^{\mathrm{L}}/\lambda)$. These are positive because we apply background corrections only (the two negative values are for lines which happen to have $I_{\mathrm{c}}^{\mathrm{AV}} < I_{\mathrm{c}}^{\mathrm{L}}$); corrections for single blends are implicitly present by our use of half profiles for asymmetric lines. The latter are shown by dots, the 154 whole-profile lines by crosses.

The lines are well distributed over line strength and wavelength; although there are many more lines to choose from in the blue, these are also more often rejected. The $\log \lambda$ panel shows the effect of the line-haze correction at left. There is also a slight increase in spread at right, where the continuum ratio $I_{\mathrm{c}}^{\mathrm{L}}/I_{\mathrm{c}}^{\mathrm{T}}$ tends to be close to unity (Fig. 4); it is due to the increase of the background corrections with wavelength, for a given continuum ratio. The scatter does not reach the full range of figure 2 because the selection and halving criteria above pass only smaller background deviations. The corrections are very small. The exact location of the true continuum is therefore not very important; the deficiencies of the Ardeberg-Virdefors continuum and the uncertainty in the size of the violet line haze do not strongly affect our results below.

The middle panels show the corrections of MMH. These are the differences $\Delta_{\mathrm{MMH}} \equiv \log(W_{\mathrm{MMH}}^{\mathrm{T}}/\lambda) - \log(W_{\mathrm{MMH}}^{\mathrm{L}}/\lambda)$ as specified by them : $W_{\mathrm{MMH}}^{\mathrm{L}}$ is given in column 2 of MMH in mÅ, $W_{\mathrm{MMH}}^{\mathrm{T}}/\lambda$ in column 3 in Fraunhofer; we have converted these into the logarithmic line strengths used here. There are two different groups of lines. The wedge-shaped concentration aligned with $\Delta_{\mathrm{MMH}} = 0$ in the lefthand panel represents lines with small or no explicit MMH corrections; the widening of the wedge towards the left is primarily due to the 0.1 Fraunhofer discretization of the $W_{\mathrm{MMH}}^{\mathrm{T}}/\lambda$ values.

The lines outside the wedge have large explicit MMH corrections. These must have resulted from the mixture of background corrections, blend corrections and the weighted averaging with other values from the literature described in section 2 and 3 of MMH (see also Houtgast and Minnaert, 1951). Positive and negative corrections occur about equally. The positive corrections may have been for background errors, for which MMH used a correcting procedure in principle like ours (their Fig. 5 shows properties of the curves in Fig. 2). The negative corrections may have been for recognised blends, candidates being the slight blends in the lines which we have halved. However, there is no correlation between the MMH corrections and our background corrections (plot not shown), there is no clear distinction between the dots and the crosses, and the size of the MMH corrections is an order of magnitude larger than ours (note the difference in vertical scale). We show below that most of these large MMH corrections for clean lines have probably resulted from the averaging with other determinations. Their increase in number towards the right illustrates that the stronger lines were better covered in the literature at the time.

The $\log \lambda$ panel (middle right) shows a pattern of slanted lines also due to the coarse MMH discretization for the weakest lines. The stronger lines show a predominance of negative corrections in the red part of the spectrum.

The bottom panels show the differences between the corrected MMH values and our corrected values. They represent to a large extent a direct display of MMH errors, owing to the superior quality of the Jungfraujoch Atlas. Their spread decreases from about 0.6 dex for the weakest lines to 0.2 dex ($\pm$ 25 %) for the stronger lines (lefthand panel). The spread in the errors is twice the spread in the MMH corrections above; however, the latter have helped : a similar plot with the uncorrected values (not shown) has appreciably larger dispersion at right.

All weak lines at left are arranged in a slanted fringe pattern which is again due to the MMH discretization. Its spacing decreases from 0.3 dex (100 %) at lower left until it is no longer traceable near $\log(W/\lambda) = -5.5$.

There are a slight predominance of positive errors at left and of negative errors at right, which affect the mean and will therefore affect abundance values determined from MMH equivalent widths; the best lines are those between $\log(W/\lambda) = -5.5$ and $\log(W/\lambda) = -5.0$.

The $\log \lambda$ panel (bottom right) shows properties noted also in figure 9 of paper RZ but left unexplained there : an upward spread, and a mean dip at $\log \lambda = 2.80$. Comparison with figure 9 RZ shows that the pattern includes also another dip at $\log \lambda = 2.83$, a mean hump around $\log \lambda = 2.85$, and an upward spike at $\log \lambda = 2.68$. The similarity confirms the conclusion by RZ that the deviations from the Fe I curve of growth plotted there are primarily due to errors in the MMH values. The upward spread is now seen to be due to the weakest lines (bottom-left panel); the spike-dip-dip-hump wavelength pattern consists of stronger lines. The pattern is yet clearer in a similar plot (not shown) with the uncorrected MMH line strengths; it is also present in the MMH corrections (middle-right panel), but upside-down and at smaller amplitude. This indicates that the pattern must be attributed to the MMH equivalent-width measurements W^{L}_{MMH}, and that the MMH corrections have partially erased it.

In figure 7, we plot the MMH corrections Δ_{MMH} against what they should have been, for the stronger lines with $\log(W/\lambda) > -5.5$ only. The dots show a clear trend with slope 0.5, showing that their MMH corrections should have been about twice their actual MMH value. The dots represent the lines for which MMH averaged their measurement W^{L}_{MMH} with other values from the literature, prior to applying their background and blend corrections. The other lines (crosses) cluster around $\Delta_{MMH} = 0$, showing that the latter corrections were generally small, as they indeed should for clean lines; note, however, that the *errors* range over 0.2 dex. Assuming that the MMH background and blend corrections were small also for most of the lines represented by dots leads to the conclusion that the trend results from the averaging alone. It then follows that many of the values from the literature used in the MMH weighting were actually much better than the MMH measurements.

Finally, we have identified four deviating lines in figure 7. The first three are marked as blended in MMH; they have nevertheless passed our rejection criteria because the blends are separated by more than 3 pm.

4. The clean Fe I lines.

4.1 The NLTE formation of high-excitation Fe I lines. — We now discuss only the lines of table IV which are due to Fe I and for which *gf* values have been published by the Kiev workers (Gurtovenko and Kostik, 1981; 302 lines) or by the Oxford group (Blackwell *et al.*, 1982, and references therein; 14 lines). The Oxford *gf*-values are precise laboratory measurements. The Kiev *gf*-values are based on empirical LTE fits of the depths of the lines in the Jungfraujoch Atlas. They offer the advantage of supplying just the lines needed; their disadvantage is that they are subject to modelling errors, most notably the erroneous assumption of LTE. Nevertheless, their quality is surprisingly good; this has been explained in paper RK (for a summary see Rutten, 1983).

In the meantime, Wiese (1983) has shown that the Kiev *gf*-values are appreciably too large above $\log gf = -1$, continuing the trend already indicated above $\log gf = -2$ in figure 1 RZ. This result is of special interest because it settles the issue of the formation of high-excitation Fe I lines, which we briefly elaborate here.

The most-probable Fe I transitions ($\log gf > -1$) in the visible are also the strongest high-excitation lines in the solar spectrum, with upper levels at $\chi = 5.5$-6.7 eV (Fig. 3 RK and Fig. 2 RZ). The excesses of their Kiev *gf*-values imply that their source functions drop below the Planck function, confirming inferences in papers RK and RZ and the theoretical predictions by Athay and Lites (1972) and Lites (1972). The reason is simply that the strongest lines at high excitation are weak enough to « feel » the solar surface already in the photosphere, in contrast to the much stronger large-*gf* lines at low excitation which maintain the excitation balance up to the chromosphere. On the other hand, the large-*gf* high-excitation lines are still strong enough that their photon losses, rather than the continuous processes, set their upper-level populations and the populations of nearby collisionally-coupled levels. These high-level populations are apparently not coupled strongly to the LTE population of the Fe II ground state, presumably not collisionally because the energy difference yet exceeds 1 eV (Fig. 2 RZ) and not radiatively because most levels ionize to a much higher Fe II parent term. (If the high Fe I levels had LTE populations, the source functions of the high-excitation lines would *exceed* the Planck function and the Kiev *gf*-values would be too small).

Thus, the important processes in Fe I are the radiative overionization shared by all levels, and the underexcitation due to photon losses in the most-probable transitions per upper-level excitation bin; the latter departures start deeper if the most-probable lines in a bin are weaker. Photon losses affect the *photospheric* populations therefore only for high levels. As a result, *all* photospheric Fe I lines have opacity deficits compared to LTE predictions, but the stronger high-excitation lines have source function deficits as well. This clarifies claims, based on the apparent self-consistency of LTE modelling, that high-excitation lines are closer to LTE than low-excitation lines (e.g., Ruland *et al.*, 1980). For the sun the reverse is true; but, misleadingly, the decreases in line depth caused by the NLTE opacity deficits are partially cancelled by the NLTE source function deficits for high-excitation lines and not for low-excitation lines. However, if the opacity deficits are already cancelled by the adoption of an opacity-shifted NLTE-masking photospheric model, the high-excitation source function deficits yet stand out. This is the case for the Kiev line-depth fits, which are based on the Holweger-Müller (1974) model; for both the sun and Pollux, adoption of a Bell *et al.* (1976) model leads to similar masking (Fig. 1 RK; Ruland *et al.*, 1980).

4.2 The Fe I curve of growth. — In figure 8 (top) we show curves of growth constructed for the 316 clean Fe I lines following the NLTE recipe of paper RZ. The abscissae measure $\log X = \log gf - (\log gf_6 + 6)$. The normalization term $\log gf_6$ was determined for each line from its wavelength and lower-level excitation energy by double cubic-spline interpolation in table 1 RZ.

The curve on the left is for the corrected MMH line strengths (column 3 of MMH). It represents a subset of the curve of growth of paper RZ for the clean lines only. It does not reach the damping part because there are no stronger lines fully free from blends. The MMH discretization is apparent at the lower left.

The spread is shown in detail in the lefthand bottom panel of figure 8. The ordinate ΔX measures the horizontal deviation of each point of the empirical curve in the top panel from the standard $\lambda = 550$ nm theoretical curve of paper RZ, similarly to figure 7 RZ. Deviations to the left are taken positive. The spread is smallest for $-5.5 < \log X < -5.0$; it increases towards both sides.

The panels on the right are the corresponding plots using our corrected line strengths of table IV. The curve of growth (top panel) is of appreciably better quality. The spread (bottom panel) is again smallest for $-5.5 < \log X < -5.0$; it is here about three times better than in the lefthand panel. The butterfly pattern of increasing scatter left and right is yet clearer; we analyse each wing separately.

4.3 THE SPREAD OF THE WEAK LINES. — Below $\log X = -5.5$ there is an increase of the spread for the weakest lines, but only downwards; it reaches as much as -0.3 dex. This part of the curve of growth has no predicted forkings since the normalization terms $\log gf_6$ neutralize its dependence on wavelength and excitation energy explicitly. Our equivalent-width determinations are better than 0.02 dex for unblended lines and quasi-continuous blending, while single, yet uncorrected blends cause upward shifts; thus, we seek positive errors in some particular Kiev gf-values exceeding their typical spread of 0.1 dex. The erroneous values are all for less-probable lines (triangles), without the NLTE error discussed above.

It turns out that these large deviations for weak lines are simply due to a measurement error : Gurtovenko and Kostik have apparently measured the line depths directly from the nominal $I = 100$ level of the graphical Jungfraujoch Atlas, instead of measuring them from the local continuum and applying background corrections $D^{\mathrm{T}} - D^{\mathrm{L}}$. In addition, the Atlas $I = 100$ level is probably higher than the true continuum, except in the violet (Fig. 4). These line-depth errors have translated directly into the gf errors measured by ΔX, because the Kiev gf-value of a weak line scales linearly with the adopted line depth.

Figure 9a illustrates this diagnosis. It shows the deviations of all lines on the Doppler part of the curve of growth against $\log (D^{\mathrm{T}}/D^{\mathrm{JJ}})$. D^{JJ} is the line depth measured from the Atlas $I = 100$ level; D^{T} is the « true » line depth found from our local depth D^{L} by adopting the same true continuum as in section 3.1, and applying corrections $D^{\mathrm{T}} - D^{\mathrm{L}}$ derived from table II. ($D^{\mathrm{T}}/D^{\mathrm{L}} = W^{\mathrm{T}}/W^{\mathrm{L}}$ for weak lines.) There is a clear correlation; the slope of the dashed fit is nearly unity, proving that indeed the nominal $I = 100$ level was used. The fit has $\Delta X = -0.01$ for $D^{\mathrm{T}} = D^{\mathrm{JJ}}$; this systematic offset from the RZ theoretical curve of growth is an error of the latter, caused by the predominance of positive MMH errors for the weak lines evident in the bottom-left panel of figure 6.

In addition, there are a few weak lines with large positive deviations; they are identified in figure 8.

4.4 THE SPREAD OF THE STRONG LINES. — Figure 9b shows the ΔX values of all lines with $\log X > -4.8$ against $\log \lambda$. These are all from the flat part of the curve of growth and have various dependencies and errors. The predicted flat part depends sensitively on the adopted microturbulence and has appreciable wavelength and damping forkings. The wavelength forking causes offsets ranging from $+0.2$ dex at left to -0.3 dex at right. The damping forking should cause upward offsets for strong lines with large orbitals (large symbols). The most-probable Kiev lines (circles) should have downward NLTE-error offsets. The Kiev background error diagnosed above for the weakest lines is negligible for lines of intermediate strength, but it affects the strongest lines also because line-core saturation makes the fitted gf-value very sensitive to small errors in the measured line depth (see Fig. 8 of Gurtovenko and Kostik); this error also causes downward offsets. Finally, some lines may have upward offsets due to uncorrected blends.

The confusion arising from these offsets is smallest for the Oxford lines (crosses), which have small gf errors and orbitals and should display primarily the wavelength forking. The dashed curve is a least-square fit through these 12 lines only; it does indeed mimic the predicted wavelength forking (Fig. 7 RZ), except that it is displaced by about -0.07 dex. The Kiev lines show much more scatter, but follow the predicted offsets by and large; the best lines (small triangles) appear to have a smaller downward offset than the Oxford lines.

4.5 RECALIBRATION OF THE KIEV gf-VALUES. — We attribute the difference between the Oxford lines and the best Kiev lines in figure 9b to an error in the absolute calibration of the Kiev gf-values. Gurtovenko and Kostik have put their gf values on the Oxford absolute scale by adjusting the average of 21 lines of overlap. Lines with the NLTE error, lines with the background error and line-core blends have all, if present, contributed too large values to this average, resulting in underestimation for the correct Kiev lines. In figure 10 we replot the current set of 50 lines of overlap shown also in figure 1 RZ, again excluding $\lambda 499.41$ and $\lambda 772.32$. We have inspected these lines in the Jungfraujoch Atlas and measured line depths and equivalent widths for the best half of each line as in section 3.1. The plusses in figure 10 mark lines the core of which is clearly affected by a nearby blend; the crosses mark the only weak lines in this sample, both showing the background error; the triangles mark NLTE-error lines with $\log gf > -2.0$. The abscissa is a measure of the strong-line background error, the core saturation being measured by $X/(W/\lambda)$.

The plusses, crosses, triangles and the two dots at right all appear to be displaced downward in accordance with their assorted errors; taking the mean over the remaining lines leads to a revision of the absolute scale of the Kiev gf-values by $+0.03 \pm 0.02$ dex. Together with the -0.01 dex offset of the fit in figure 9a, an offset of -0.04 dex results for the Oxford lines from the RZ theoretical curve of growth, which was shifted to fit the weak-line MMH line strengths to the Kiev gf-values. The mean offset of the 12 Oxford lines in figure 9b is somewhat larger, perhaps implying correction of the microturbulence adopted by RZ.

4.6 THE SOLAR IRON ABUNDANCE. — The iron abundance enters through the normalization terms gf_6 which are inversely proportional to the value adopted in their computation; the value used by RZ is $A_{\mathrm{Fe}} = N_{\mathrm{Fe}}/N_{\mathrm{H}} = 4.73 \times 10^{-5}$. The ΔX values of figures 8 and 9 represent direct corrections to this number, provided that the other factors have been eliminated.

We refrain from using the strong lines. Accepting the fit in figure 9a and the recalibration derived from figure 10 leads to an average correction of -0.04 dex. We therefore revise the solar iron abundance to $A_{\rm Fe} = (4.3 \pm 0.5)\ 10^{-5}$, or $A_{\rm Fe}^{12} \equiv \log A_{\rm Fe} + 12 = 7.63 \pm 0.04$, maintaining the RZ error estimate. For consistency all values of $\log gf_6$ in table 1 RZ should be increased by 0.04.

4.7 OSCILLATOR STRENGTHS OF WEAK Fe I LINES. — In table VI we provide new estimates for the oscillator strengths of the 258 Fe I lines present in table IV that have $\log (W/\lambda) < -5.2$; these include 39 new lines not measured at Kiev or Oxford. We have determined their gf values by evaluating the three theoretical curves of growth given in figure 6a RZ for the measured line strength and interpolating to the line wavelength by cubic spline. The values have been shifted to the Oxford absolute scale over the + 0.04 dex correction found above.

Thus, the gf values in table VI are based on our measured line strengths and on the assumption that Lites' NLTE modelling of the Fe I spectrum, which has been confirmed in papers RK and RZ in general, is precisely correct. These gf values are therefore quite similar to the empirical Kiev determinations in origin, but they should be of better precision because we have explicitly included background corrections and NLTE departures. However, they are yet subject to the remaining blends and the remaining modelling errors; we suspect that the simplified description of the solar granulation by micro- and macroturbulence is the worst of the latter.

5. Conclusion.

We have supplied consumer reports on the quality of the Jungfraujoch Atlas (Figs. 4 and 5), of the MMH equivalent widths (Figs. 6 and 7) and of the Kiev gf-values (Figs. 9 and 10); we have further supplied a detailed recipe for background corrections (Table II), a list of 750 clean solar lines (Table IV), a list of 258 Fe I gf-values (Table VI) ([2]), the best-ever solar curve of growth (Fig. 8), and, traditionally, a new value for the solar iron abundance. We intend to compile a companion list of the same clean lines as measured in the solar flux spectrum (Rutten and van der Zalm, 1984, vol. 55, n° 2).

We now summarize our results in a wider context, together with those of papers RK and RZ. We do this because the solar spectrum and the Fe I spectrum are the best-observed spectra of all stellar spectra and of all metal spectra respectively, and because Fe I is also the spectral species best represented in the solar spectrum (Table V). An analysis of solar Fe I lines therefore represents a feasibility study for analyzing other cool stars and other metals, making it appropriate to summarize this series of papers on solar Fe I in the context of stellar abundance determination in general. Following the model of a feasibility study we pattern the discussion on different levels of desired precision, namely 100 % (0.3 dex), 25 % (0.1 dex) and 5 % (0.02 dex). These are defined per line; averaging over many lines may help but only if there are no systematic errors, which is difficult to ascertain if the desired precision is not reached per line.

We first discuss the issue of *observational stellar data*. Conventional photographic spectrography of MMH-like quality yields line strengths with errors of 0.3 dex for the weakest lines (Fig. 6). The stronger lines are better, but above $\log (W/\lambda) = -5.2$ they are increasingly spoiled by the various forkings of the curve of growth (Fig. 8 and Fig. 6 RZ). The best unbiased lines are near $\log (W/\lambda) = -5.5$; they have errors of about 0.1 dex (Fig. 6 bottom and Fig. 8).

Digital photoelectric spectrometry of Jungfraujoch Atlas quality yields line strengths better than 0.02 dex for clean lines. The main problem is the continuum location. The true continuum is not easily found (Figs. 4 and 5), and it is completely hidden where unresolved blends combine into a line haze (Sect. 2.2); however, the background corrections are small (Fig. 6 top). Proper location of the local continuum is more important (Fig. 9a); this requires sufficient spectral purity. For dirtier lines the extraction of blends requires detailed spectral synthesis to reach 0.02 dex precision.

The next issue is the *description of the line formation*. For Fe I and similar spectra, simple LTE curve-of-growth interpretation suffices for a precision of 0.3 dex, but 0.1 dex requires correction of the departures from LTE in the ionization equilibrium (Fig. 3 RZ). A satisfactory shortcut is to use a single set of height-dependent population correction factors for all levels if one omits the strongest high-excitation lines (Sect. II RK). A further shortcut in solar analyses is to assume LTE and the NLTE-masking photospheric model of Holweger and Müller (1974) (Paper RK and Fig. 3 RZ). In stellar analyses adoption of a theoretical LTE-RE model from the compilation by Bell *et al.* (1976) may constitute a similar shortcut (Fig. 1 RK; Ruland *et al.*, 1980).

A precision better than 0.02 dex requires detailed modelling of individual line profiles, full solution of the radiative transfer and population equations for many lines and levels, and adoption of a realistic empirical model of the atmosphere. Furthermore, the questionable description of motions and inhomogeneities by turbulence, the formalisms of collisional damping, and the details of frequency redistribution should then receive full consideration. The outstanding example remains Lites' (1972) thesis, on which these papers are based.

The final issue concerns the *laboratory data*. We consider only the line transition probabilities, neglecting all other cross-sections needed in comprehensive modelling. A major result of these papers is that the empirical Kiev determinations are highly useful. They combine 0.1 dex precision [except for the weakest and the strongest lines (Figs. 9 and 10), and for the most-probable lines (Sect. 4.1)] with the important virtue of supplying precisely the weak lines needed in abundance studies. We have revised their absolute calibration; improved values are given in table VI for the weak lines.

Better than 0.02 dex precision is reached in the Oxford laboratory data, which complement the Kiev lines with the stronger lines (Fig. 4 RZ). These are precisely the lines needed in comprehensive model-atom setups.

([2]) Copies of these tables on magnetic tape or punched cards can be obtained from E.v.d.Z.

To sum up, the desired precision divides the three issues naturally in three recipes. The classical basis (photographic line strengths, LTE, older gf values) is good for 0.3 dex. For 0.1 dex one has to combine photoelectric line strengths of weak lines with Kiev-type gf-values in a NLTE curve of growth. Finally, 0.02 dex requires full NLTE modelling of detailed profiles of strong lines and Oxford-type gf-values. *It is not worthwhile to spend effort on one issue without seeking the concomitant sophistication in the others.*

Acknowledgements.

We thank Drs. C. Zwaan and A. Schadee for suggestions and for comments on the paper.

References

ARDEBERG, A., VIRDEFORS, B. : 1975, *Astron. Astrophys.* **45,** 19.
ARDEBERG, A., VIRDEFORS, B. : 1979, *Astron. Astrophys. Suppl. Ser.* **36,** 317.
ATHAY, R. G., LITES, B. W. : 1972, *Astrophys. J.* **176,** 809.
BELL, R. A., ERIKSSON, K., GUSTAFSSON, B., NORDLUND, Å. : 1976, *Astron. Astrophys. Suppl. Ser.* **23,** 37.
BLACKWELL, D. E., PETFORD, A. D., SHALLIS, M. J., SIMMONS, G. J. : 1982, *Mon. Not. R. Astron. Soc.* **199,** 43.
BRAULT, J. W. : 1978, in « Future Solar Optical Observations : Needs and Constraints », eds. G. Godoli, G. Noci, A. Righini, *Osserv. Mem. Oss. Astrofis. Arcetri* **106,** 33.
CRAM, L. E., RUTTEN, R. J., LITES, B. W. : 1980, *Astrophys. J.* **241,** 374.
DELBOUILLE, L., ROLAND, G., NEVEN, L. : 1973, *Photometric Atlas of the Solar Spectrum from λ3000 to λ10000,* Institut d'Astrophysique, Liège.
DRAVINS, D., LINDEGREN, L., NORDLUND, Å. : 1981, *Astron. Astrophys.* **96,** 345.
ELSTE, G. : 1978, in *High Resolution Spectrometry,* ed. M. Hack, 4th Trieste Colloquium, 692.
ENARD, D. : 1981, *The Messenger,* E.S.O. No. 26, p. 22.
GURTOVENKO, E. A., KOSTIK, R. I. : 1981, *Astron. Astrophys. Suppl. Ser.* **46,** 239.
GRIFFIN, R. F. : 1968, *A Photometric Atlas of the Spectrum of Arcturus,* Cambridge Philosophical Society, Cambridge U.K.
GRIFFIN, R. E., GRIFFIN, R. : 1979, *A Photometric Atlas of the Spectrum of Procyon,* Institute of Astronomy, Cambridge U.K.
HOLWEGER, H. : 1970, *Astron. Astrophys.* **4,** 11.
HOLWEGER, H., MÜLLER, E. A. : 1974, *Sol. Phys.* **39,** 19.
HOUTGAST, J., MINNAERT, M. G. J. : 1951, *Rech. Obs. Utrecht* **12,** part II.
KURUCZ, R. L., PEYTREMANN, E., AVRETT, E. H. : 1974, *Blanketed Model Atmospheres for Early-Type Stars,* Smithsonian Institution Press, Washington.
LABS, D., NECKEL, H. : 1970, *Sol. Phys.* **15,** 79.
LITES, B. W. : 1972, *NCAR Cooperative Thesis No. 28,* University of Colorado and High Altitude Observatory, NCAR, Boulder.
LITES, B. W., WHITE, O. R. : 1973, *High Altitude Observatory Research Memorandum* No. 185, Boulder.
MIHALAS, D. : 1970, *Stellar Atmospheres* (Freeman and Co., San Francisco).
MINNAERT, M. G. J., MULDERS, G. F. W., HOUTGAST, J. : 1940, *Photometric Atlas of the Solar Spectrum from λ3612 to λ8771,* Sterrewacht « Sonnenborgh », Utrecht.
MOORE, Ch. E., MINNAERT, M. G. J., HOUTGAST, J. : 1966, « The Solar Spectrum 2935 Å to 8770 Å », *Nat. Bur. Stand. (U.S.), Monogr.,* No. 61, Washington.
POWELL, D. R., MACDONALD, J. R. : 1972, *Comput. J.* **15,** 148.
RULAND, F., HOLWEGER, H., GRIFFIN, R., GRIFFIN, R., BIEHL, D. : 1980, *Astron. Astrophys.* **92,** 70.
RUTTEN, R. J. : 1983, in *Highlights of Astronomy,* ed. R. M. West, **6,** p. 801.
RUTTEN, R. J., CRAM, L. E. : 1981, in *The Sun as a Star,* Ed. S. D. Jordan, CNRS-NASA Monograph Series on Nonthermal Phenomena in Stellar Atmospheres, NASA SP-450, part IV.
RUTTEN, R. J., KOSTIK, R. I. : 1982, *Astron. Astrophys.* **115,** 104 (Paper RK).
RUTTEN, R. J., ZWAAN, C. : 1983, *Astron. Astrophys.* **117,** 21 (Paper RZ).
VERNAZZA, J. E., AVRETT, E. H., LOESER, R. : 1976, *Astrophys. J. Suppl. Ser.* **30,** 1.
WARNER, B. : 1969, *Observatory* **89,** 11.
WIESE, W. L. : 1983, in *Highlights of Astronomy,* ed. R. M. West, **6,** p. 795.

TABLE I. — *Computed continuum ratios I_c^L/I_c^T as function of the continuous opacity increment ε and the wavelength λ (nm).*

λ \ ε	0.02	0.03	0.05	0.075	0.10	0.15
400	0.9854	0.9783	0.9644	0.9746	0.9315	0.9010
500	0.9882	0.9824	0.9711	0.9575	0.9444	0.9196
600	0.9902	0.9855	0.9762	0.9649	0.9541	0.9336
700	0.9917	0.9877	0.9798	0.9702	0.9610	0.9535
800	0.9928	0.9892	0.9823	0.9740	0.9659	0.9507

TABLE III. — *Extended Ardeberg-Virdefors continuum I_c^{AV} for the Jungfraujoch Atlas, specified by the wavelengths (nm) and intensities (Atlas units) of the polygon junction points.*

Wavelength	Intensity	Wavelength	Intensity
400.600	9903.3	620.061	9919.0
431.722	9919.0	645.324	9912.5
445.477	9919.0	686.000	9910.2
460.736	9936.6	700.040	9888.0
474.087	9913.8	702.950	9889.3
482.270	9933.0	746.790	9885.8
493.309	9934.9	773.830	9892.5
507.382	9922.7	800.000	9892.5
537.125	9931.7		
544.225	9928.3		
565.012	9954.9		
579.751	9928.4		
594.036	9929.5		
603.296	9946.2		
611.472	9939.5		

TABLE II. — *Functional approximation to all Fe I background-correction curves. The correction*

$$\Delta x_1 = \log(W^T/\lambda) - \log(W^L/\lambda)$$

is given by :

$$\Delta x_1 = c_7 - 0.5\, c_5 \tanh(c_1(x_1 - c_2)) + 1 - c_6 \exp(((x_1 - c_3)/c_4)^2)$$

where, for $i = 1, \ldots, 7$:

$$c_i = a_i + b_i\, x_4\,,$$
$$a_i = d_{i,1} + d_{i,2}\, x_2 + (d_{i,3} + d_{i,4}\, x_2)\, x_3\,,$$
$$b_i = d_{i,5} + d_{i,6}\, x_2 + (d_{i,7} + d_{i,8}\, x_2)\, x_3\,.$$

The coefficients $d_{i,j}$ are given below ; the variables x_i are the observed parameters, respectively : $x_1 = \log(W^L/\lambda)$, x_2 = wavelength λ in nm, x_3 = lower-level excitation energy χ in eV, x_4 = continuum ratio I_c^L/I_c^T.

$d_{i,j}$	j = 1	j = 2	j = 3	j = 4	j = 5	j = 6	j = 7	j = 8
i = 1	3.549	-1.545E-3	-3.593E-1	5.429E-4	-2.297	2.800E-3	5.010E-1	-7.405E-4
i = 2	-4.745	-2.129E-3	-4.342E-2	-2.927E-5	-6.142E-1	1.376E-3	3.250E-2	8.134E-5
i = 3	-4.605	-1.145E-3	6.874E-3	-5.474E-5	-2.610E-1	7.973E-4	9.335E-3	2.374E-5
i = 4	3.273E-1	9.203E-5	7.870E-3	-1.061E-5	4.227E-2	-5.519E-5	-1.357E-2	2.052E-5
i = 5	-1.082E-2	5.765E-5	-8.471E-3	5.836E-5	1.084E-2	-5.777E-5	8.426E-3	-5.835E-5
i = 6	-6.903E-2	2.527E-4	4.450E-3	2.056E-5	6.899E-2	-2.529E-4	-4.481E-3	-2.054E-5
i = 7	-2.801E-1	1.047E-3	-1.041E-2	1.385E-4	2.798E-1	-1.048E-3	1.031E-2	-1.385E-4

TABLE IV.

Wavelength	Ident	Mode	D^L	FWHM	$\log(W/\lambda)^L$	I_c^L/I_c^T	$\log(W/\lambda)^T$
401.3232	Ti Ip 186	W	0.097	5.82	-5.806	0.9279	-5.794
402.1332	Nd II 36	B	0.225	4.69	-5.544	0.9269	-5.533
404.1913	Fe I 602	B	0.175	5.29	-5.615	0.9244	-5.600
404.2583	Ce II 140	B	0.199	4.79	-5.597	0.9341	-5.586
405.0323	Zr II 43	B	0.367	5.35	-5.267	0.9368	-5.258
406.0266	Ti I 80	W	0.561	5.94	-5.039	0.9356	-5.033
408.5720	Zr II 54	R	0.065	5.07	-6.075	0.9159	-6.058
409.1556	Fe I 357	W	0.765	6.77	-4.845	0.9410	-4.837
419.4490	Fe I 274	W	0.278	5.65	-5.395	0.9383	-5.384
426.5920	Mn I 23	B	0.720	7.60	-4.854	0.9381	-4.845
426.6208	Ti I 252	R	0.102	5.95	-5.821	0.9393	-5.808
428.1374	Ti I 44	B	0.377	5.76	-5.248	0.9327	-5.240
428.1594	Fe Ip 171	B	0.115	5.24	-5.819	0.9341	-5.806
431.9445	Fe I 214	B	0.214	5.90	-5.503	0.9434	-5.492
434.9787	Ce II 59	W	0.085	6.05	-5.888	0.9557	-5.878
436.4886	Cr I 153	B	0.015	5.86	-6.691	0.9524	-6.678
439.2302	Fe Ip 757	R	0.094	7.95	-5.717	0.9461	-5.704
441.0523	Ni I 88	R	0.616	7.94	-4.869	0.9558	-4.862
441.3392	Fe Ip 1046	B	0.089	7.69	-5.760	0.9629	-5.750
443.9639	Fe I 515	W	0.275	6.00	-5.383	0.9560	-5.374
443.9887	Fe I 116	W	0.661	6.77	-4.954	0.9574	-4.948
444.1271	Ti I 160	W	0.104	5.38	-5.877	0.9481	-5.867
444.4393	Ce II 19	B	0.055	4.73	-6.218	0.9542	-6.207
444.5476	Fe I 2	R	0.572	5.81	-5.087	0.9537	-5.083
444.6392	Nd II 49	B	0.171	5.15	-5.674	0.9577	-5.665
445.0091	Ni I 178	W	0.054	5.32	-6.168	0.9458	-6.153
446.5809	Ti I 146	W	0.493	6.69	-5.076	0.9544	-5.070
447.0482	Ni I 86	B	0.793	9.36	-4.723	0.9586	-4.715
448.5971	Fe Ip 825	W	0.258	6.29	-5.400	0.9621	-5.391
449.1658	Cr I 95	R	0.277	6.76	-5.340	0.9569	-5.332
449.1850	Cr I 83	W	0.140	6.10	-5.691	0.9589	-5.681
449.2307	Cr I 197	B	0.339	6.88	-5.238	0.9655	-5.231
450.4212	Fe Ip 988	B	0.025	6.25	-6.423	0.9689	-6.414
450.5919	Y I 24	R	0.021	6.91	-6.481	0.9671	-6.474
451.2272	Ca I 24	R	0.273	7.24	-5.303	0.9662	-5.297
451.2740	Ti I 42	B	0.761	7.94	-4.822	0.9663	-4.818
451.2994	Ni I 163	R	0.246	6.85	-5.367	0.9669	-5.360
451.8027	Ti I 42	R	0.794	8.04	-4.787	0.9647	-4.782
452.3079	Ce II 2	k	0.173	6.12	-5.565	0.9615	-5.556
452.3404	Fe I 829	R	0.536	6.96	-5.029	0.9654	-5.023
454.3223	Fe Ip 893	R	0.046	6.03	-6.183	0.9620	-6.172
454.6470	Fe I 1047	B	0.083	6.23	-5.885	0.9578	-5.872
454.8768	Ti I 42	R	0.787	7.87	-4.811	0.9559	-4.805
455.1650	Fe I 972	B	0.352	6.57	-5.269	0.9590	-5.260
455.6929	Fe I 638	R	0.328	6.64	-5.244	0.9622	-5.237
456.0715	V I 109	B	0.118	6.21	-5.763	0.9659	-5.755
456.2632	Ti I 7	R	0.149	6.16	-5.627	0.9718	-5.623
456.3423	Ti I 266	R	0.132	6.80	-5.676	0.9566	-5.666
456.6025	Fe Ip 1169	R	0.008	6.42	-6.840	0.9678	-6.829
456.7410	Ni I 102	W	0.042	6.78	-6.161	0.9699	-6.153
457.4220	Fe I 554	R	0.480	7.20	-5.065	0.9696	-5.060
457.5111	Cr I 196	B	0.129	6.57	-5.699	0.9700	-5.691
459.2052	Cr II 44	B	0.521	8.53	-4.980	0.9718	-4.973
459.3528	Fe I 971	W	0.339	7.03	-5.221	0.9715	-5.215
460.7087	Fe Ip 724	W	0.047	6.16	-6.165	0.9717	-6.157
462.2747	Cr I 81	B	0.245	6.81	-5.412	0.9541	-5.402
462.5919	Cr I 244	R	0.154	6.81	-5.609	0.9562	-5.597
462.9067	Zr II 139	B	0.041	6.26	-6.228	0.9693	-6.217
463.0779	Fe I 969	W	0.043	5.67	-6.242	0.9668	-6.232
463.3259	Cr I 186	W	0.119	6.16	-5.761	0.9683	-5.752
465.8299	Fe I 591	B	0.203	6.56	-5.516	0.9640	-5.507
467.0172	Fe II 25	R	0.335	7.33	-5.234	0.9565	-5.223
467.2837	Fe Ip 40	B	0.370	7.76	-5.154	0.9627	-5.149
469.0797	Ti I 76	B	0.046	5.52	-6.261	0.9640	-6.254
470.0613	Cr I 62	B	0.208	6.39	-5.517	0.9639	-5.509
470.6304	Fe Ip 890	R	0.092	6.40	-5.850	0.9593	-5.838
470.8016	Cr I 186	R	0.627	8.24	-4.919	0.9552	-4.911
470.9497	Ru I 14	B	0.026	6.89	-6.399	0.9773	-6.394
470.9713	Mn I 21	R	0.675	9.26	-4.832	0.9774	-4.828
471.6838	Fe I 634	R	0.076	6.35	-5.938	0.9646	-5.928
472.0134	Fe IIp 54	B	0.048	8.18	-6.020	0.9795	-6.012
472.2161	Zn I 2	B	0.697	9.04	-4.799	0.9809	-4.795
472.2761	Cr I 195	B	0.025	5.71	-6.470	0.9638	-6.459
472.6141	Fe I 384	R	0.210	6.22	-5.498	0.9674	-5.490
473.7353	Cr I 145	R	0.593	8.14	-4.938	0.9684	-4.933
474.3822	Sc I 14	B	0.076	9.30	-5.790	0.9817	-5.787
474.5131	Fe I 67	B	0.158	6.02	-5.669	0.9671	-5.661
474.6117	Co I 182	B	0.020	7.42	-6.500	0.9737	-6.492
474.8733	La II 65	B	0.053	6.18	-6.106	0.9798	-6.101
475.4360	Co I 156	R	0.070	8.10	-5.898	0.9630	-5.887
475.7841	Ru I 12	B	0.022	7.87	-6.406	0.9791	-6.401
475.8121	Ti I 233	B	0.525	7.35	-5.060	0.9766	-5.056
475.8420	Ni I 193	W	0.037	7.29	-6.212	0.9760	-6.205
475.9273	Ti I 233	R	0.564	7.47	-4.997	0.9827	-4.994
476.0065	Fe I 384	R	0.085	5.80	-5.955	0.9674	-5.946
476.7858	Cr I 231	B	0.212	6.80	-5.481	0.9839	-5.477
477.0672	Cr I 124	R	0.045	7.91	-6.060	0.9645	-6.049
477.3966	Ce II 17	R	0.108	7.22	-5.744	0.9704	-5.736
477.5140	Cr I 230	B	0.070	7.26	-5.930	0.9818	-5.925
477.7854	Sm II 3	B	0.012	5.54	-6.840	0.9802	-6.836
477.8258	Ti I 232	B	0.182	7.11	-5.490	0.9833	-5.486
477.9443	Fe I 720	R	0.507	6.95	-5.078	0.9823	-5.075
478.0812	Fe I 633	B	0.099	6.62	-5.811	0.9761	-5.805
478.7494	Fe Ip 408	R	0.023	6.76	-6.455	0.9808	-6.449
478.8761	Fe I 588	B	0.713	8.48	-4.833	0.9818	-4.830
479.0562	Fe I 1068	W	0.102	6.52	-5.821	0.9741	-5.813
479.0745	Fe I 632	R	0.104	6.75	-5.795	0.9786	-5.789
479.1600	Sm II 7	R	0.035	6.99	-6.266	0.9815	-6.261
479.2858	Co I 158	W	0.368	7.66	-5.175	0.9829	-5.172
479.3424	Ni I 158	R	0.051	7.55	-6.039	0.9834	-6.034
479.3969	Fe I 512	B	0.097	6.71	-5.824	0.9853	-5.820
479.4360	Fe I 115	B	0.139	6.48	-5.651	0.9842	-5.648
479.4824	Ti IIp 29	B	0.025	7.74	-6.363	0.9835	-6.358
479.8267	Fe I 1042	R	0.498	7.36	-5.066	0.9723	-5.060
479.9066	Fe Ip 1098	B	0.039	7.01	-6.198	0.9832	-6.193
480.1028	Cr I 168	B	0.558	7.88	-5.001	0.9766	-4.997
480.2527	Fe I 1206	R	0.163	7.48	-5.523	0.9786	-5.517
480.5874	Zr I 43	B	0.011	6.76	-6.682	0.9805	-6.678
480.8152	Fe I 633	W	0.334	6.81	-5.267	0.9730	-5.262
480.9941	Fe I 793	B	0.227	7.01	-5.434	0.9766	-5.428
481.3480	Co I 158	B	0.456	8.67	-5.043	0.9811	-5.040
482.0415	Ti I 126	R	0.468	7.40	-5.091	0.9818	-5.088
483.5871	Fe I 1068	R	0.555	7.83	-5.014	0.9780	-5.010
483.6854	Cr I 144	B	0.167	7.22	-5.557	0.9728	-5.550
483.7400	Ti Ip 250	B	0.026	7.54	-6.375	0.9858	-6.371
488.0058	Cr I 167	B	0.065	8.50	-5.919	0.9798	-5.913
488.5435	Fe I 966	R	0.721	8.67	-4.835	0.9694	-4.828
489.2861	Fe I 1070	B	0.546	8.47	-4.974	0.9772	-4.970
490.5137	Fe I 986	B	0.356	7.21	-5.202	0.9737	-5.197
490.8610	Fe I 115	R	0.082	6.43	-5.920	0.9775	-5.914
491.3976	Ni I 132	R	0.601	8.03	-4.928	0.9787	-4.924
491.5235	Ti I 157	W	0.086	6.48	-5.907	0.9802	-5.902
491.7234	Fe I 1066	B	0.649	8.68	-4.899	0.9751	-4.893
492.6153	Ti I 39	R	0.078	6.74	-5.910	0.9888	-5.908
493.5835	Ni I 177	R	0.631	8.46	-4.895	0.9851	-4.892
493.6340	Cr I 166	B	0.498	7.85	-5.071	0.9791	-5.067
495.3212	Ni I 111	R	0.588	8.19	-4.937	0.9888	-4.934
495.3719	Cr I 166	R	0.059	7.18	-6.019	0.9909	-6.017
495.4304	Fe Ip 1093	B	0.020	6.76	-6.488	0.9838	-6.483
496.1920	Fe I 845	B	0.294	7.35	-5.324	0.9881	-5.322
496.2577	Fe I 1097	R	0.582	8.09	-4.946	0.9836	-4.942
496.4720	Ti I 173	B	0.099	6.71	-5.824	0.9868	-5.821
496.4932	Cr I 9	B	0.469	6.97	-5.152	0.9821	-5.149
496.6814	Cr I 259	R	0.034	9.92	-6.155	0.9828	-6.149
496.7528	Ni I 141	R	0.161	7.29	-5.574	0.9783	-5.568
497.6697	Ni Ip 254	W	0.073	6.89	-5.958	0.9860	-5.954
498.7624	Fe Ip 1094	W	0.037	6.96	-6.242	0.9876	-6.237
499.2786	Fe I 1110	B	0.107	7.69	-5.730	0.9880	-5.726
499.3353	Fe II 36	B	0.422	8.16	-5.120	0.9898	-5.118
499.5411	Fe I 1113	R	0.159	7.20	-5.592	0.9788	-5.585
499.5655	Ni I 145	B	0.214	7.13	-5.465	0.9788	-5.459
500.3739	Ni I 50	B	0.402	6.85	-5.221	0.9891	-5.219
500.4893	Mn I 20	B	0.152	7.69	-5.596	0.9913	-5.594
501.0941	Ni I 144	R	0.549	7.81	-5.011	0.9897	-5.009
501.6477	Fe I 1089	B	0.370	7.53	-5.214	0.9881	-5.212
502.2867	Ti I 38	B	0.738	8.92	-4.845	0.9858	-4.843
502.6483	Ni I 158	B	0.030	7.46	-6.336	0.9861	-6.331
504.7117	Fe Ip 1242	R	0.050	7.36	-6.122	0.9792	-6.114
504.8846	Ni I 195	R	0.633	8.57	-4.887	0.9798	-4.882
505.8494	Fe I 884	B	0.147	6.78	-5.665	0.9933	-5.663
506.2100	Ti I 199	B	0.172	7.83	-5.531	0.9905	-5.529
506.4060	Ti I 294	R	0.066	7.46	-5.946	0.9929	-5.945
507.1486	Ti I 110	B	0.265	9.32	-5.285	0.9844	-5.283
509.4410	Ni I 164	R	0.357	7.43	-5.231	0.9933	-5.229
511.2485	Cr I 19	B	0.042	6.08	-6.290	0.9910	-6.288
511.3439	Ti I 109	B	0.312	7.14	-5.327	0.9909	-5.326
511.9906	Fe Ip 960	R	0.051	7.69	-6.066	0.9941	-6.064
512.2116	Cr I 19	B	0.138	6.36	-5.735	0.9877	-5.732
513.2931	Ti I 230	B	0.022	7.52	-6.467	0.9856	-6.463
513.7934	Cr I 207	B	0.023	7.52	-6.448	0.9866	-6.444
514.1739	Fe I 114	B	0.768	10.41	-4.736	0.9962	-4.736
514.5462	Ti I 109	R	0.417	7.57	-5.177	0.9903	-5.175
514.5733	Fe Ip 931	R	0.046	10.68	-5.960	0.9946	-5.959
515.2183	Ti I 4	R	0.436	6.92	-5.190	0.9892	-5.189
515.7977	Ni I 111	B	0.219	7.31	-5.466	0.9932	-5.465
515.9947	Fe Ip 1095	R	0.054	7.03	-6.101	0.9921	-6.098
518.7908	Fe I 1032	R	0.564	8.11	-4.971	0.9860	-4.968
519.6057	Fe I 1091	R	0.690	9.25	-4.841	0.9841	-4.837
519.7158	Ni I 204	B	0.275	8.04	-5.317	0.9956	-5.316
520.0167	Cr I 201	B	0.231	8.69	-5.358	0.9923	-5.356
520.5287	Fe Ip 1112	W	0.027	6.55	-6.438	0.9808	-6.430
520.6808	Fe Ip 1095	R	0.066	7.47	-5.966	0.9897	-5.962
521.0040	Co I 167	B	0.024	6.97	-6.447	0.9853	-6.442
521.3804	Fe I 962	B	0.084	6.85	-5.923	0.9894	-5.919
521.4126	Cr I 193	B	0.203	7.26	-5.512	0.9917	-5.510
521.9699	Ti I 4	R	0.302	6.94	-5.338	0.9950	-5.337
522.3182	Fe I 880	B	0.339	7.25	-5.282	0.9911	-5.280
523.0970	Ti I 215	W	0.020	7.32	-6.517	0.9911	-6.515
523.4622	Fe II 49	W	0.720	10.51	-4.779	0.9852	-4.774
523.7316	Cr II 43	W	0.510	9.41	-4.991	0.9914	-4.988
523.8243	Fe I 962	W	0.031	8.47	-6.255	0.9971	-6.255
523.8958	Cr I 59	B	0.189	7.18	-5.537	0.9978	-5.537
524.0870	V I 131	W	0.045	11.55	-5.974	0.9963	-5.973
524.1450	Cr I 59	W	0.041	7.26	-6.208	0.9950	-6.206
524.3779	Fe I 1089	R	0.618	8.69	-4.927	0.9909	-4.925
524.7287	Ti I 183	B	0.098	6.95	-5.851	0.9841	-5.847
524.9996	Co I 190	R	0.037	8.16	-6.242	0.9733	-6.231
525.0210	Fe I 1	R	0.709	8.01	-4.921	0.9819	-4.918
525.3020	Fe Ip 113	B	0.232	6.46	-5.498	0.9927	-5.496
525.4645	Co I 187	B	0.055	7.91	-6.071	0.9813	-6.064
525.5510	Nd II 43	B	0.087	5.41	-6.025	0.9781	-6.019
525.9727	Pr II 35	B	0.039	6.80	-6.262	0.9960	-6.261
525.9968	Ti I 298	W	0.072	7.56	-5.958	0.9920	-5.956
526.2619	Fe Ip 1149	R	0.111	7.92	-5.734	0.9904	-5.731
526.4802	Fe II 48	W	0.484	8.78	-5.045	0.9946	-5.044
527.9652	Fe Ip 584	B	0.050	7.27	-6.094	0.9981	-6.094
528.0628	Co I 172	R	0.167	9.52	-5.471	0.9963	-5.470
528.2396	Ti I 74	R	0.193	9.68	-5.378	0.9864	-5.375
528.7172	Cr I 225	B	0.118	7.73	-5.710	0.9981	-5.709
528.7780	Co I 187	W	0.033	7.57	-6.298	0.9815	-6.291

TABLE IV *(continued)*.

Wavelength	Ident		Mode	D^L	FWHM	$\log(W/\lambda)^L$	I_c^L/I_c^T	$\log(W/\lambda)^T$
528.9820	Y II	20	B	0.044	6.99	-6.200	0.9941	-6.198
529.3370	Cr I	192	B	0.052	7.04	-6.134	0.9970	-6.133
529.4540	Fe I	875	B	0.164	7.11	-5.623	0.9913	-5.620
529.5306	Fe I	1146	W	0.321	7.80	-5.276	0.9922	-5.274
529.5771	Ti I	74	R	0.138	7.18	-5.649	0.9926	-5.647
529.9978	Ti I	74	W	0.162	10.83	-5.428	0.9923	-5.427
530.0394	Fe I	1240	B	0.047	8.08	-6.108	0.9949	-6.107
530.0745	Cr I	18	B	0.611	8.39	-4.984	0.9903	-4.982
530.1312	Fe Ip	1162	B	0.030	7.96	-6.313	0.9963	-6.312
530.3218	V II	54	B	0.036	9.94	-6.154	0.9945	-6.152
530.4178	Cr I	225	R	0.167	8.06	-5.530	0.9962	-5.529
530.5865	Cr II	24	B	0.264	8.53	-5.325	0.9965	-5.324
530.8426	Cr II	43	B	0.253	9.21	-5.328	0.9952	-5.327
530.8681	Fe I	1091	B	0.070	6.80	-5.998	0.9870	-5.993
531.0687	Cr II	43	R	0.133	8.46	-5.624	0.9930	-5.621
531.1626	Hf II	37	R	0.030	7.53	-6.327	0.9912	-6.324
531.2645	Co I	197	B	0.071	7.48	-5.976	0.9924	-5.973
531.2852	Cr I	225	R	0.208	7.75	-5.462	0.9931	-5.460
531.8351	Sc II	22	B	0.120	9.03	-5.655	0.9959	-5.654
531.8763	Cr I	225	W	0.171	7.52	-5.570	0.9938	-5.568
532.0032	Fe I	877	B	0.218	7.17	-5.486	0.9894	-5.483
532.1109	Fe I	1165	R	0.436	8.11	-5.095	0.9931	-5.093
532.5270	Co I	192	W	0.088	7.87	-5.840	0.9799	-5.833
532.5548	Fe II	49	R	0.446	8.56	-5.077	0.9859	-5.073
532.6812	Fe I	1147	B	0.130	8.36	-5.661	0.9858	-5.656
533.6162	Co I	191	B	0.031	7.79	-6.324	0.9850	-6.318
534.2703	Co I	190	B	0.331	8.20	-5.235	0.9977	-5.235
534.4758	Cr I	225	R	0.089	7.65	-5.835	0.9976	-5.835
534.7710	Ni I	145	B	0.056	7.17	-6.075	0.9929	-6.073
534.8319	Cr I	18	R	0.784	11.34	-4.718	0.9935	-4.717
535.2048	Co I	172	W	0.188	10.04	-5.426	0.9888	-5.423
535.6089	Sc I	17	R	0.018	9.14	-6.455	0.9967	-6.454
535.7184	Sc II	30	B	0.040	6.83	-6.236	0.9942	-6.234
535.8111	Fe Ip	628	R	0.106	7.11	-5.788	0.9933	-5.786
535.9194	Co I	194	W	0.102	8.01	-5.785	0.9932	-5.783
537.6827	Fe I	1132	B	0.173	7.30	-5.599	0.9947	-5.597
537.7050	La II	95	B	0.045	7.07	-6.198	0.9924	-6.195
537.9574	Fe I	928	R	0.621	8.67	-4.928	0.9952	-4.927
538.0316	C I	11	B	0.157	14.26	-5.354	0.9927	-5.352
538.4629	Ti I	35	R	0.016	7.53	-6.621	0.9968	-6.620
538.5132	Zr I	26	B	0.020	7.96	-6.503	0.9978	-6.503
538.6330	Fe I	1064	B	0.353	7.82	-5.244	0.9934	-5.242
538.9481	Fe I	1145	R	0.716	10.05	-4.801	0.9852	-4.797
539.2328	Ni I	250	B	0.134	7.57	-5.674	0.9916	-5.671
539.5216	Fe I	1143	B	0.225	7.52	-5.446	0.9939	-5.444
539.8280	Fe I	1145	R	0.670	9.42	-4.866	0.9879	-4.863
540.1265	Fe I	1146	B	0.272	7.62	-5.376	0.9944	-5.374
540.2775	Y II	35	B	0.137	6.91	-5.709	0.9913	-5.706
540.6776	Fe I	1148	R	0.387	8.04	-5.160	0.9915	-5.158
541.2786	Fe Ip	1162	R	0.203	7.53	-5.491	0.9892	-5.488
541.7036	Fe I	1148	R	0.360	7.99	-5.193	0.9937	-5.191
542.2149	Fe Ip	1145	R	0.113	7.66	-5.743	0.9916	-5.740
542.5246	Fe II	49	R	0.425	8.72	-5.086	0.9940	-5.085
542.6241	Ti I	3	B	0.073	6.91	-5.965	0.9947	-5.964
543.6290	Fe I	1161	B	0.417	8.23	-5.147	0.9947	-5.145
543.8028	Fe I	1237	B	0.025	8.87	-6.378	0.9971	-6.377
543.8298	Ti I	108	W	0.030	9.13	-6.281	0.9908	-6.278
544.3402	Fe Ip	1059	B	0.033	9.34	-6.215	0.9958	-6.213
544.8907	Ti I	259	R	0.015	7.66	-6.619	0.9941	-6.617
546.4279	Fe I	1030	R	0.407	7.94	-5.168	0.9919	-5.166
546.8105	Ni I	192	B	0.139	7.55	-5.656	0.9959	-5.655
547.0089	Fe I	1144	B	0.267	8.21	-5.333	0.9954	-5.331
547.1199	Ti I	106	B	0.087	7.15	-5.902	0.9974	-5.902
547.2285	Ce II	24	R	0.020	6.28	-6.592	0.9907	-6.589
547.3387	Y II	27	B	0.067	7.12	-6.032	0.9840	-6.026
547.4224	Ti I	108	R	0.112	7.11	-5.797	0.9888	-5.794
547.4453	Ti I	259	R	0.036	8.44	-6.228	0.9953	-6.227
548.4619	Sc I	16	B	0.031	9.09	-6.230	0.9987	-6.230
549.0150	Ti I	107	B	0.242	7.10	-5.466	0.9934	-5.465
549.1829	Fe I	1031	R	0.129	7.92	-5.665	0.9949	-5.663
549.4464	Fe I	1024	B	0.280	7.73	-5.350	0.9863	-5.346
549.9407	Ni I	176	R	0.022	8.09	-6.466	0.9932	-6.464
549.9587	Fe Ip	1159	R	0.029	7.61	-6.332	0.9968	-6.331
550.3893	Ti I	287	B	0.151	7.47	-5.666	0.9871	-5.662
550.6485	Mo I	4	W	0.038	6.35	-6.329	0.9741	-6.322
552.0490	Sc I	15	B	0.076	8.51	-5.894	0.9977	-5.894
552.1281	Fe Ip	1162	B	0.059	6.58	-6.124	0.9855	-6.118
552.2442	Fe I	1108	W	0.453	8.27	-5.117	0.9907	-5.115
552.4244	Fe I	1059	R	0.044	7.32	-6.192	0.9941	-6.190
552.6813	Sc II	31	B	0.687	10.22	-4.852	0.9931	-4.851
553.7104	Ni I	188	B	0.033	7.56	-6.269	0.9961	-6.268
553.9278	Fe I	871	W	0.184	7.51	-5.530	0.9876	-5.526
554.6989	Fe I	1061	B	0.249	8.17	-5.370	0.9842	-5.365
555.2221	Sc II	25	R	0.043	8.94	-6.139	0.9945	-6.137
555.2687	Fe Ip	1281	B	0.081	8.04	-5.877	0.9964	-5.876
556.0209	Fe I	1164	B	0.528	8.86	-5.033	0.9932	-5.031
556.8862	Fe I	869	B	0.112	7.14	-5.812	0.9909	-5.809
557.7023	Fe I	1314	R	0.117	8.34	-5.687	0.9937	-5.685
557.8722	Ni I	47	R	0.550	8.63	-5.013	0.9921	-5.012
558.7571	Fe I	1026	B	0.377	8.10	-5.228	0.9785	-5.222
558.7859	Ni I	70	R	0.582	8.37	-5.004	0.9861	-5.001
558.9360	Ni I	205	R	0.289	8.12	-5.318	0.9929	-5.316
559.3733	Ni I	206	B	0.425	8.72	-5.097	0.9957	-5.096
559.5051	Fe Ip	1314	W	0.062	8.23	-5.981	0.9890	-5.976
560.6999	Ni I	205	B	0.033	7.84	-6.311	0.9918	-6.308
560.8976	Fe Ip	1108	W	0.102	8.21	-5.756	0.9870	-5.751
560.9965	Fe Ip	866	R	0.050	8.46	-6.075	0.9887	-6.071
561.1357	Fe Ip	869	B	0.099	7.37	-5.829	0.9930	-5.827
561.8634	Fe I	1107	W	0.509	8.64	-5.061	0.9864	-5.057
561.9597	Fe I	1161	W	0.338	8.50	-5.232	0.9925	-5.230
562.2215	Si I	11	R	0.040	10.11	-6.091	0.9932	-6.088
562.8643	Cr I	203	W	0.151	8.13	-5.604	0.9945	-5.602
563.5821	Fe I	1088	B	0.360	8.27	-5.225	0.9929	-5.223
563.6700	Fe I	868	B	0.221	7.59	-5.492	0.9968	-5.492
563.8745	Ni I	203	R	0.094	7.85	-5.824	0.9901	-5.820
564.1439	Fe I	1087	R	0.569	10.83	-4.917	0.9832	-4.912
564.2364	Cr I	239	B	0.054	8.70	-6.037	0.9923	-6.034
564.3078	Ni I	259	W	0.158	8.18	-5.587	0.9927	-5.585
564.4356	Fe Ip	1057	B	0.016	8.09	-6.542	0.9844	-6.535
564.6110	V I	37	R	0.032	10.72	-6.191	0.9942	-6.189
564.7238	Co I	112	W	0.121	9.67	-5.641	0.9965	-5.640
564.8262	Cr I	239	W	0.040	8.76	-6.151	0.9942	-6.149
564.8565	Ti I	269	W	0.107	7.88	-5.776	0.9945	-5.774
564.9385	Cr I	239	B	0.068	8.66	-5.937	0.9929	-5.935
564.9991	Fe I	1314	R	0.360	8.75	-5.181	0.9899	-5.178
565.1469	Fe Ip	1161	B	0.195	7.89	-5.523	0.9943	-5.521
565.2316	Fe I	1108	B	0.271	8.20	-5.348	0.9931	-5.346
565.7443	V I	37	W	0.051	8.61	-6.070	0.9979	-6.069
566.1017	Fe Ip	1234	B	0.043	7.81	-6.173	0.9925	-6.170
566.1343	Fe I	1108	R	0.232	8.11	-5.400	0.9960	-5.399
566.2153	Ti I	249	B	0.226	7.66	-5.490	0.9813	-5.485
566.5557	Si I	10	R	0.326	11.30	-5.112	0.9932	-5.111
567.0850	V I	36	R	0.151	11.07	-5.498	0.9955	-5.497
567.7689	Fe Ip	1057	B	0.070	7.82	-5.963	0.9945	-5.961
567.8388	Fe Ip	982	R	0.048	8.14	-6.088	0.9909	-6.084
567.9921	Ti I	269	B	0.054	7.67	-6.095	0.9922	-6.093
568.0244	Fe I	1026	R	0.111	8.35	-5.729	0.9951	-5.727
568.6836	Sc I	12	R	0.082	8.75	-5.848	0.9882	-5.845
569.0425	Si I	10	B	0.417	10.89	-5.042	0.9884	-5.038
570.1104	Si I	10	R	0.328	10.61	-5.170	0.9930	-5.168
570.1550	Fe I	209	R	0.711	10.52	-4.828	0.9925	-4.826
570.2314	Cr I	203	W	0.213	10.37	-5.375	0.9974	-5.374
570.2650	Ti I	249	B	0.079	7.71	-5.926	0.9964	-5.925
570.7260	Fe Ip	866	R	0.028	7.59	-6.404	0.9855	-6.398
571.3882	Ti I	249	W	0.038	8.25	-6.197	0.9963	-6.196
571.7834	Fe I	1107	B	0.578	9.55	-4.935	0.9866	-4.931
571.9817	Cr I	119	B	0.049	7.55	-6.126	0.9950	-6.124
572.5644	V I	135	W	0.018	9.60	-6.486	0.9958	-6.485
572.7657	V I	35	B	0.062	11.84	-5.870	0.9980	-5.870
572.9198	Cr I	257	W	0.026	8.60	-6.385	0.9986	-6.385
573.1767	Fe I	1087	R	0.560	9.17	-4.976	0.9960	-4.975
573.7068	V I	35	B	0.079	10.70	-5.808	0.9945	-5.807
573.8233	Fe I	1084	B	0.120	8.77	-5.693	0.9943	-5.691
573.9472	Ti I	228	B	0.087	7.75	-5.883	0.9963	-5.882
574.1851	Fe I	1086	W	0.317	8.61	-5.275	0.9932	-5.273
574.2963	Fe I	1084	B	0.114	7.80	-5.773	0.9882	-5.769
574.8359	Ni I	45	R	0.293	8.12	-5.315	0.9928	-5.313
575.2038	Fe I	1180	R	0.527	9.25	-5.002	0.9933	-5.000
575.4406	Fe I	866	W	0.129	7.32	-5.763	0.9758	-5.754
575.9259	Fe I	1184	B	0.085	7.89	-5.907	0.9927	-5.904
576.0342	Fe I	867	B	0.245	7.66	-5.442	0.9948	-5.440
576.0527	Fe Ip	1054	R	0.022	7.45	-6.543	0.9905	-6.539
576.0829	Ni I	231	W	0.350	8.52	-5.222	0.9905	-5.219
576.6331	Ti I	309	R	0.088	8.96	-5.792	0.9972	-5.791
577.5083	Fe I	1087	R	0.560	9.31	-4.967	0.9978	-4.967
577.8461	Fe I	209	W	0.232	7.68	-5.465	0.9961	-5.464
578.3071	Cr I	188	R	0.318	8.81	-5.233	0.9967	-5.232
578.4663	Fe I	686	B	0.274	7.89	-5.381	0.9970	-5.381
578.5984	Ti I	309	W	0.114	8.58	-5.738	0.9838	-5.732
579.3073	Si I	9	B	0.346	11.13	-5.137	0.9915	-5.134
579.3918	Fe I	1086	R	0.351	8.39	-5.223	0.9976	-5.222
579.8510	Cr I	17	R	0.016	7.85	-6.640	0.9958	-6.639
580.5218	Ni I	234	W	0.392	9.45	-5.137	0.9957	-5.136
580.6728	Fe I	1180	R	0.500	9.22	-5.038	0.9939	-5.036
580.7984	Fe Ip	1178	R	0.031	7.95	-6.318	0.9942	-6.316
580.9875	Fe Ip	1084	R	0.020	8.64	-6.492	0.9976	-6.492
581.1912	Fe I	1022	B	0.119	7.87	-5.757	0.9985	-5.757
581.2828	Ti I	309	B	0.022	8.90	-6.434	0.9958	-6.433
581.4814	Fe I	1086	W	0.235	8.33	-5.415	0.9963	-5.414
581.9930	V II	99	B	0.031	9.66	-6.252	0.9962	-6.250
582.3158	Fe II	164	W	0.018	9.69	-6.512	0.9959	-6.510
582.4416	Fe IIp	58	B	0.028	9.03	-6.342	0.9979	-6.341
582.7872	Fe Ip	552	R	0.118	7.84	-5.742	0.9963	-5.741
583.2480	Ti I	309	W	0.020	8.77	-6.492	0.9976	-6.491
583.5099	Fe Ip	1084	B	0.142	7.82	-5.684	0.9926	-5.682
583.7702	Fe I	1129	B	0.100	7.99	-5.823	0.9958	-5.822
583.8670	Cr I	119	B	0.040	8.47	-6.195	0.9954	-6.193
584.4596	Cr I	119	B	0.042	7.82	-6.219	0.9960	-6.218
584.4921	Fe I	1056	B	0.033	7.90	-6.312	0.9959	-6.310
584.6999	Ni I	44	B	0.226	7.97	-5.474	0.9979	-5.474
584.9687	Fe Ip	922	W	0.081	7.93	-5.909	0.9962	-5.907
585.2219	Fe I	1178	W	0.392	8.96	-5.147	0.9984	-5.147
585.3150	Fe I	35	B	0.077	7.63	-5.938	0.9963	-5.937
585.5084	Fe I	1179	B	0.222	8.36	-5.458	0.9952	-5.457
585.6090	Fe I	1128	B	0.340	8.67	-5.240	0.9945	-5.238
585.8776	Fe Ip	1084	B	0.130	8.65	-5.661	0.9956	-5.659
585.9590	Fe I	1181	R	0.618	10.21	-4.894	0.9893	-4.891
586.1110	Fe Ip	1084	B	0.083	8.45	-5.860	0.9986	-5.859
586.2364	Fe I	1180	W	0.659	11.60	-4.813	0.9894	-4.810
586.6454	Ti I	72	R	0.458	8.93	-5.110	0.9924	-5.108
586.7566	Ca I	46	B	0.220	9.39	-5.402	0.9946	-5.401
587.6276	Fe Ip	1084	W	0.042	7.99	-6.218	0.9892	-6.213
587.9490	Fe Ip	1201	B	0.096	8.45	-5.809	0.9932	-5.806
588.0025	Fe I	1201	W	0.116	8.42	-5.727	0.9944	-5.725
588.0268	Ti I	71	B	0.063	7.74	-6.059	0.9944	-6.058
588.1281	Fe Ip	1178	R	0.144	8.64	-5.610	0.9931	-5.608
588.3823	Fe I	982	W	0.579	10.39	-4.928	0.9877	-4.925
588.4441	Cr I	119	B	0.029	8.76	-6.334	0.9908	-6.330
590.2472	Fe I	1234	B	0.142	8.10	-5.669	0.9965	-5.668
590.3318	Ti I	71	B	0.047	7.61	-6.178	0.9947	-6.176

TABLE IV *(continued)*.

Wavelength	Ident	Mode	D^L	FWHM	$\log(W/\lambda)^L$	I_c^L/I_c^T	$\log(W/\lambda)^T$
590.5674	Fe I 1181	R	0.532	9.64	-4.988	0.9955	-4.987
590.6497	Ti I 105	B	0.050	8.84	-6.091	0.9969	-6.090
592.2119	Ti I 72	W	0.198	8.17	-5.515	0.9959	-5.514
592.7785	Fe I 1175	B	0.410	9.43	-5.134	0.9978	-5.133
592.9678	Fe I 1176	B	0.386	9.04	-5.188	0.9902	-5.185
593.0182	Fe I 1180	W	0.668	11.67	-4.811	0.9867	-4.806
593.3805	Fe Ip 1198	B	0.059	9.84	-5.966	0.9948	-5.964
593.4662	Fe I 982	W	0.618	10.91	-4.879	0.9907	-4.876
594.7531	Fe I 1199	B	0.083	9.10	-5.850	0.9962	-5.849
594.8544	Si I 16	R	0.576	12.93	-4.819	0.9910	-4.816
595.6702	Fe I 14	B	0.538	8.39	-5.090	0.9969	-5.089
596.9567	Fe I 1086	R	0.040	8.83	-6.196	0.9956	-6.195
597.6169	Fe Ip 1125	B	0.015	8.36	-6.637	0.9973	-6.636
597.6786	Fe I 959	W	0.571	10.15	-4.967	0.9798	-4.961
597.8546	Ti I 154	W	0.238	8.19	-5.447	0.9930	-5.446
598.2854	Cr I 185	B	0.033	8.96	-6.296	0.9957	-6.294
598.4823	Fe I 1260	B	0.634	12.07	-4.817	0.9909	-4.814
599.1363	Fe II 46	R	0.293	9.52	-5.269	0.9933	-5.267
599.6729	Ni I 249	W	0.186	9.02	-5.506	0.9897	-5.502
600.0660	Co I 169	R	0.028	11.86	-6.203	0.9937	-6.201
600.3017	Fe I 959	W	0.646	11.39	-4.852	0.9827	-4.847
600.7965	Fe I 1178	R	0.540	9.76	-4.991	0.9830	-4.985
600.8561	Fe I 982	R	0.663	11.44	-4.820	0.9878	-4.816
601.5242	Fe Ip 63	W	0.045	7.73	-6.212	0.9947	-6.211
601.6643	Mn I 27	B	0.626	14.84	-4.776	0.9925	-4.774
601.9369	Fe Ip 780	B	0.048	9.36	-6.065	0.9963	-6.064
602.5760	Ni I 251	W	0.042	9.98	-6.118	0.9980	-6.118
602.7055	Fe I 1018	B	0.596	10.05	-4.972	0.9875	-4.968
603.4037	Fe Ip 1142	W	0.081	8.22	-5.920	0.9922	-5.917
603.9729	V I 34	W	0.130	7.91	-5.721	0.9945	-5.720
605.3687	Ni I 247	R	0.180	8.92	-5.524	0.9860	-5.519
605.4077	Fe I 1142	B	0.090	8.26	-5.859	0.9907	-5.855
605.6008	Fe I 1259	B	0.608	11.25	-4.892	0.9945	-4.890
606.4633	Ti I 69	B	0.080	7.88	-5.938	0.9930	-5.936
606.5490	Fe I 207	B	0.753	14.22	-4.713	0.9851	-4.708
606.7608	Si I 15	R	0.024	12.25	-6.263	0.9979	-6.263
607.8495	Fe I 1259	B	0.611	11.02	-4.879	0.9924	-4.877
607.9013	Fe I 1176	R	0.434	9.50	-5.091	1.0001	-5.092
608.1447	V I 34	B	0.128	8.94	-5.695	0.9942	-5.693
608.4106	Fe II 46	B	0.202	9.32	-5.479	0.9982	-5.478
608.6285	Ni I 249	R	0.394	9.83	-5.126	0.9960	-5.125
608.6675	Co I 165	B	0.023	12.42	-6.322	0.9957	-6.320
608.9570	Fe I 1327	R	0.350	8.81	-5.219	0.9960	-5.218
609.0215	V I 34	R	0.322	8.84	-5.277	0.9945	-5.275
609.1181	Ti I 238	B	0.146	8.23	-5.657	0.9954	-5.656
609.3148	Co I 37	B	0.065	11.31	-5.884	0.9953	-5.883
609.3647	Fe I 1177	B	0.299	8.96	-5.317	0.9939	-5.315
609.4376	Fe I 1177	B	0.188	8.76	-5.494	0.9953	-5.492
609.6669	Fe I 959	R	0.357	9.04	-5.198	0.9969	-5.197
609.7087	Fe Ip 64	B	0.023	7.71	-6.506	0.9961	-6.505
609.8249	Fe Ip 1200	B	0.154	8.55	-5.626	0.9943	-5.624
609.8663	Ti I 304	B	0.051	9.02	-6.085	0.9949	-6.084
611.1078	Ni I 230	R	0.317	9.51	-5.243	0.9964	-5.242
611.1658	V I 34	W	0.084	11.61	-5.752	0.9987	-5.751
611.8098	Ni I 230	B	0.023	10.05	-6.403	0.9971	-6.402
612.0258	Fe I 14	B	0.051	7.92	-6.135	0.9943	-6.133
612.1007	Ti I 153	R	0.033	9.23	-6.252	0.9912	-6.248
612.5029	Si I 30	W	0.227	11.92	-5.273	0.9926	-5.270
612.6223	Ti I 69	R	0.220	8.13	-5.469	0.9958	-5.468
612.8979	Ni I 42	W	0.261	7.86	-5.427	0.9936	-5.426
612.9221	Cr II 105	R	0.021	10.22	-6.422	0.9941	-6.418
613.0140	Ni I 248	R	0.214	8.80	-5.476	0.9936	-5.473
613.3970	Ni I 229	W	0.047	9.53	-6.090	0.9969	-6.089
613.5367	V I 34	B	0.085	9.67	-5.839	0.9912	-5.837
614.3201	Zr I 2	R	0.011	10.38	-6.568	0.9929	-6.567
614.5020	Si I 29	R	0.290	11.93	-5.181	0.9945	-5.179
614.9248	Fe II 74	R	0.345	10.00	-5.187	0.9926	-5.184
615.1622	Fe I 62	W	0.507	8.57	-5.105	0.9976	-5.104
615.5699	Si I 29	R	0.051	11.00	-6.003	0.9922	-5.999
615.6789	O I 10	R	0.038	12.25	-6.086	0.9955	-6.083
615.7405	Fe Ip 624	R	0.028	8.87	-6.371	0.9923	-6.368
615.7732	Fe I 1015	B	0.569	10.04	-5.000	0.9923	-4.998
615.9383	Fe I 1175	B	0.115	9.00	-5.713	0.9952	-5.711
616.0750	Na I 5	B	0.426	11.87	-5.046	0.9870	-5.043
616.5364	Fe I 1018	R	0.442	8.98	-5.127	0.9938	-5.125
616.6439	Ca I 20	R	0.582	10.72	-4.921	0.9964	-4.920
617.3342	Fe I 62	R	0.622	9.67	-4.924	0.9974	-4.923
617.6818	Ni I 228	W	0.529	11.02	-4.964	0.9938	-4.963
617.7249	Ni I 58	W	0.144	7.91	-5.692	0.9916	-5.690
617.7556	Ni Ip 244	R	0.019	10.27	-6.448	0.9971	-6.447
618.6716	Ni I 229	B	0.276	9.51	-5.329	0.9952	-5.327
618.7402	Fe Ip 342	B	0.034	8.38	-6.254	0.9941	-6.251
618.7994	Fe I 959	R	0.432	9.71	-5.098	0.9964	-5.097
619.9509	Fe I 208	R	0.039	8.82	-6.213	1.0000	-6.213
620.0320	Fe I 207	B	0.631	10.62	-4.931	0.9959	-4.930
620.4610	Ni I 226	B	0.202	9.05	-5.485	0.9969	-5.484
621.3436	Fe I 62	W	0.667	11.13	-4.878	0.9922	-4.876
621.3869	V I 20	B	0.039	9.48	-6.202	0.9917	-6.200
621.6360	V I 19	W	0.292	10.44	-5.246	0.9950	-5.245
622.0475	Ti I 293	R	0.086	8.48	-5.877	0.9939	-5.875
622.0781	Fe I 958	B	0.175	8.69	-5.564	0.9937	-5.562
622.3989	Ni I 228	B	0.257	9.42	-5.376	0.9941	-5.374
622.4508	V I 20	B	0.052	8.58	-6.109	0.9973	-6.109
622.6740	Fe I 981	R	0.271	8.99	-5.339	0.9976	-5.338
623.0094	Ni I 227	B	0.176	9.04	-5.555	0.9880	-5.550
623.2647	Fe I 816	W	0.640	11.55	-4.857	0.9941	-4.855
623.3197	V I 20	R	0.037	9.08	-6.225	0.9962	-6.224
623.9362	Sc I 2	B	0.062	9.38	-5.988	0.9944	-5.987
623.9942	Fe II 74	R	0.109	9.34	-5.746	0.9865	-5.738
624.0652	Fe I 64	R	0.487	8.67	-5.116	0.9958	-5.115
624.2826	V I 19	B	0.075	9.99	-5.898	0.9966	-5.898
624.3113	V I 19	B	0.240	10.18	-5.383	0.9938	-5.382
624.5619	Sc II 28	B	0.301	9.94	-5.287	0.9949	-5.285
625.1823	V I 19	W	0.112	10.66	-5.685	0.9961	-5.685
625.2563	Fe I 169	R	0.741	14.34	-4.708	0.9950	-4.707
625.8110	Ti I 104	W	0.493	9.22	-5.097	0.9964	-5.096
626.5139	Fe I 62	W	0.677	11.28	-4.870	0.9931	-4.868
627.0232	Fe I 342	R	0.500	9.07	-5.081	0.9926	-5.079
627.4658	V I 19	W	0.069	8.81	-5.961	0.9967	-5.961
628.5168	V I 19	W	0.095	8.24	-5.857	0.9977	-5.857
629.0548	Fe Ip 208	B	0.040	7.84	-6.270	0.9934	-6.267
630.0683	Sc II 28	B	0.055	9.14	-6.063	0.9973	-6.062
630.3466	Fe I 1140	W	0.044	9.06	-6.139	0.9980	-6.138
630.3765	Ti I 104	W	0.075	8.42	-5.938	0.9993	-5.938
631.1505	Fe I 342	R	0.278	8.22	-5.387	0.9913	-5.384
631.5816	Fe I 1014	B	0.398	9.18	-5.199	0.9961	-5.198
631.6583	Ni I 248	B	0.030	9.80	-6.299	0.9947	-6.297
632.0418	La II 19	R	0.037	10.79	-6.127	0.9973	-6.126
632.0841	Sc II 28	B	0.069	10.01	-5.926	0.9980	-5.926
632.2171	Ni I 249	R	0.156	9.42	-5.576	0.9959	-5.574
632.2693	Fe I 207	W	0.634	10.86	-4.914	0.9952	-4.913
632.6845	V I 84	B	0.017	9.00	-6.586	0.9983	-6.586
632.7608	Ni I 44	W	0.360	9.08	-5.228	0.9988	-5.228
633.0096	Cr I 6	R	0.267	8.11	-5.397	0.9992	-5.397
633.0852	Fe I 1254	B	0.316	9.22	-5.291	0.9949	-5.290
633.5336	Fe I 62	R	0.711	12.05	-4.809	0.9921	-4.807
633.6103	Ti I 103	B	0.052	8.25	-6.125	0.9953	-6.124
635.3837	Fe Ip 13	B	0.012	7.85	-6.750	0.9936	-6.748
636.9462	Fe II 40	R	0.171	10.14	-5.502	0.9971	-5.501
637.6192	Fe Ip 1140	B	0.015	10.13	-6.517	0.9944	-6.514
637.8256	Ni I 247	B	0.277	10.07	-5.315	0.9955	-5.313
638.0747	Fe I 1015	B	0.472	9.94	-5.089	0.9930	-5.087
638.5722	Fe Ip 1253	R	0.098	9.37	-5.777	0.9967	-5.775
639.2543	Fe I 109	B	0.171	8.10	-5.626	0.9968	-5.625
639.3610	Fe I 168	R	0.735	15.47	-4.686	0.9844	-4.680
641.1108	Fe I 1256	R	0.043	8.16	-6.232	0.9801	-6.220
641.6923	Fe II 74	B	0.357	10.65	-5.187	0.9955	-5.186
642.9895	Co I 81	B	0.024	12.01	-6.315	0.9964	-6.314
643.2683	Fe II 40	B	0.363	10.44	-5.195	0.9970	-5.194
643.6411	Fe I 1016	B	0.093	8.65	-5.840	0.9968	-5.839
644.0937	Mn I 39	W	0.050	9.85	-6.071	0.9984	-6.071
645.2316	V I 48	R	0.049	13.93	-5.946	0.9979	-5.946
645.5000	Co I 174	B	0.088	13.69	-5.698	0.9963	-5.697
645.6387	Fe II 74	B	0.523	11.47	-4.993	0.9941	-4.990
646.4670	Ca I 19	B	0.112	8.82	-5.773	0.9963	-5.772
647.1663	Ca I 18	R	0.680	11.84	-4.848	0.9958	-4.847
647.7858	Co I 174	R	0.029	10.85	-6.283	0.9971	-6.281
648.1877	Fe I 109	W	0.572	9.94	-5.015	0.9932	-5.013
648.2807	Ni I 66	W	0.363	9.69	-5.215	0.9976	-5.214
649.8946	Fe I 13	W	0.440	8.62	-5.194	0.9895	-5.192
649.9654	Ca I 18	R	0.649	11.68	-4.870	0.9962	-4.869
650.8837	Ca I 18	R	0.082	9.24	-5.866	0.9975	-5.865
651.6087	Fe II 40	R	0.455	10.98	-5.055	0.9957	-5.054
651.8374	Fe I 342	B	0.509	9.84	-5.079	0.9904	-5.077
653.1431	V I 48	B	0.049	10.18	-6.087	0.9981	-6.086
653.2882	Ni I 64	B	0.148	8.93	-5.652	0.9967	-5.651
653.3936	Fe I 1197	B	0.337	10.09	-5.241	0.9931	-5.239
658.6319	Ni I 64	B	0.367	9.81	-5.219	0.9948	-5.218
659.1314	Fe I 1229	B	0.095	8.73	-5.849	0.9968	-5.847
659.3879	Fe I 168	R	0.645	11.85	-4.874	0.9920	-4.872
659.8606	Ni I 249	R	0.213	10.04	-5.436	0.9973	-5.436
659.9112	Ti I 49	B	0.084	7.92	-5.958	0.9958	-5.957
660.4593	Sc II 19	R	0.314	10.06	-5.258	0.9958	-5.257
660.6954	Ti IIp 91	B	0.064	9.36	-6.009	0.9947	-6.006
660.8031	Fe I 109	W	0.170	8.29	-5.620	0.9967	-5.619
662.5029	Fe I 13	B	0.148	7.82	-5.687	0.9976	-5.687
662.7549	Fe I 1174	B	0.251	9.38	-5.397	0.9950	-5.395
663.0013	Cr I 16	R	0.056	9.19	-6.056	0.9982	-6.055
663.2445	Co I 111	R	0.057	12.46	-5.941	0.9937	-5.938
663.3755	Fe I 1197	W	0.522	10.92	-5.021	0.9733	-5.011
663.5127	Ni I 264	R	0.204	10.43	-5.440	0.9944	-5.438
666.1081	Cr I 282	B	0.108	9.64	-5.759	0.9929	-5.756
666.1333	Ni I 246	R	0.061	10.34	-5.959	0.9952	-5.956
666.7426	Fe I 168	B	0.050	8.83	-6.143	0.9980	-6.142
666.7723	Fe I 1228	B	0.081	9.50	-5.903	0.9980	-5.903
668.7499	Y I 1	W	0.032	10.65	-6.247	0.9960	-6.246
669.8671	Al I 5	W	0.155	11.70	-5.513	0.9962	-5.512
669.9142	Fe I 1228	B	0.070	9.41	-5.925	0.9958	-5.923
670.3572	Fe I 268	R	0.348	9.12	-5.265	0.9954	-5.263
670.4485	Fe I 1052	B	0.053	9.35	-6.087	0.9963	-6.085
671.0322	Fe I 34	W	0.144	8.18	-5.710	0.9947	-5.708
671.3745	Fe I 1255	R	0.189	9.72	-5.502	0.9968	-5.501
672.5358	Fe I 1052	B	0.154	9.48	-5.612	0.9944	-5.609
672.6671	Fe I 1197	B	0.403	10.64	-5.145	0.9915	-5.142
673.3157	Fe I 1195	R	0.238	9.88	-5.399	0.9958	-5.398
673.6530	Fe Ip 1122	B	0.016	10.21	-6.588	0.9981	-6.587
673.9524	Fe I 34	R	0.108	8.67	-5.792	0.9980	-5.792
674.3130	Ti I 48	R	0.155	9.47	-5.593	0.9942	-5.591
674.5965	Fe I 1005	B	0.060	9.43	-6.019	0.9977	-6.018
675.0158	Fe I 111	W	0.616	10.94	-4.960	0.9940	-4.958
675.3465	Fe Ip 1196	W	0.051	9.48	-6.112	0.9881	-6.105
675.6547	Fe Ip 1120	W	0.026	13.11	-6.281	0.9956	-6.279
676.7781	Ni I 57	R	0.632	11.27	-4.923	0.9936	-4.921
677.2321	Ni I 127	R	0.423	10.16	-5.130	0.9963	-5.129
678.6863	Fe I 1052	W	0.219	9.64	-5.454	0.9938	-5.451
679.3260	Fe I 1005	B	0.115	9.13	-5.775	0.9940	-5.772
679.6120	Fe I 1007	W	0.088	10.80	-5.809	0.9952	-5.807
679.8477	Ca I 31	B	0.046	11.04	-6.077	0.9944	-6.074
680.1869	Fe Ip 34	W	0.015	7.88	-6.750	0.9978	-6.749
680.4275	Fe I 1225	R	0.128	9.56	-5.692	0.9922	-5.688

TABLE IV *(continued)*.

Wavelength	Ident	Mode	D^L	FWHM	$\log(W/\lambda)^L$	I_c^L/I_c^T	$\log(W/\lambda)^T$
680.6849	Fe I 268	B	0.320	9.06	-5.336	0.9951	-5.335
681.0266	Fe I 1197	R	0.420	10.56	-5.122	0.9930	-5.119
681.4954	Co I 54	R	0.121	13.20	-5.597	0.9954	-5.595
682.0373	Fe I 1197	B	0.345	10.51	-5.222	0.9937	-5.220
682.4845	Fe Ip 1280	B	0.029	9.69	-6.337	0.9980	-6.336
683.3236	Fe I 1194	R	0.082	10.14	-5.845	0.9977	-5.844
683.7010	Fe I 1225	R	0.158	9.63	-5.592	0.9952	-5.590
683.9834	Fe I 205	R	0.273	9.31	-5.371	0.9946	-5.369
684.2041	Ni I 126	R	0.223	9.91	-5.432	0.9937	-5.429
684.3660	Fe I 1173	B	0.489	11.45	-5.035	0.9939	-5.033
684.8565	Si I 37	B	0.113	13.64	-5.574	0.9964	-5.572
685.0441	Ni I 157	B	0.057	13.96	-5.852	0.9952	-5.849
685.1643	Fe I 34	R	0.037	8.90	-6.275	0.9969	-6.274
685.5720	Fe I 1194	B	0.147	10.29	-5.610	0.9914	-5.606
685.7252	Fe I 1006	W	0.198	9.75	-5.496	0.9969	-5.495
685.8154	Fe I 1173	R	0.427	10.89	-5.100	0.9957	-5.099
686.0102	Fe Ip 1255	B	0.025	10.50	-6.389	0.9965	-6.387
686.1243	Ni I 293	W	0.030	9.40	-6.352	0.9918	-6.347
686.1942	Fe I 109	R	0.171	9.05	-5.586	0.9995	-5.586
686.2499	Fe I 1191	W	0.265	10.04	-5.350	0.9997	-5.350
686.4314	Fe Ip 1186	B	0.054	9.65	-6.060	0.9958	-6.058
688.0633	Fe I 1051	B	0.118	9.42	-5.743	0.9928	-5.740
688.2519	Cr I 222	B	0.264	10.41	-5.339	0.9909	-5.336
688.3058	Cr I 222	B	0.256	10.23	-5.377	0.9932	-5.375
689.8294	Fe I 1078	W	0.139	9.63	-5.658	0.9945	-5.655
691.6689	Fe I 1052	B	0.451	11.14	-5.108	0.9760	-5.099
692.5278	Cr I 222	B	0.312	10.73	-5.253	0.9958	-5.252
692.6095	Cr I 222	B	0.155	10.68	-5.545	0.9925	-5.541
693.6499	Fe I 1196	B	0.058	9.63	-6.045	0.9972	-6.043
695.1246	Fe I 1186	W	0.408	10.71	-5.142	0.9935	-5.140
695.1246	Fe I 1193	W	0.408	10.71	-5.142	0.9935	-5.140
696.0323	Fe I 1222	R	0.107	9.62	-5.795	0.9912	-5.791
697.0473	Fe Ip 463	W	0.047	10.20	-6.109	0.9982	-6.109
697.1937	Fe I 404	R	0.112	8.98	-5.789	0.9941	-5.787
697.8859	Fe I 111	W	0.612	11.51	-4.960	0.9890	-4.956
697.9798	Cr I 222	R	0.274	11.10	-5.307	0.9961	-5.305
698.0937	Cr I 222	B	0.067	9.77	-5.981	0.9945	-5.978
698.8531	Fe I 167	W	0.307	9.26	-5.341	0.9960	-5.340
699.6662	Ti I 256	B	0.024	9.45	-6.456	0.9961	-6.454
700.0621	Fe I 1005	B	0.157	9.65	-5.629	0.9964	-5.627
700.1549	Ni I 64	W	0.104	9.48	-5.805	0.9986	-5.805
700.3576	Si I 60	B	0.363	15.31	-5.037	0.9912	-5.033
700.7973	Fe I 1078	W	0.237	10.15	-5.415	0.9926	-5.412
701.0353	Fe I 1221	R	0.109	9.97	-5.758	0.9988	-5.758
702.2961	Fe I 1051	W	0.505	11.68	-5.018	0.9893	-5.014
702.4067	Fe I 1003	B	0.243	9.67	-5.441	0.9959	-5.440
703.0019	Ni I 126	W	0.179	9.57	-5.559	0.9960	-5.558
703.4377	Ni I 97	B	0.084	10.04	-5.897	0.9885	-5.891
703.8228	Fe I 1051	R	0.479	11.32	-5.037	0.9930	-5.034
705.4028	Co I 140	W	0.037	13.52	-6.126	0.9969	-6.125
706.2971	Ni I 64	R	0.123	9.77	-5.714	0.9977	-5.713
706.9538	Fe I 205	R	0.043	9.67	-6.177	0.9984	-6.177
707.0076	Sr I 3	B	0.010	9.61	-6.732	0.9952	-6.730
707.1857	Fe I 1194	B	0.184	13.35	-5.393	0.9937	-5.391
707.2812	Fe I 1003	R	0.048	10.44	-6.117	0.9956	-6.115
708.3400	Fe I 1277	B	0.188	10.04	-5.528	0.9953	-5.526
709.0394	Fe I 1051	B	0.507	11.92	-5.014	0.9934	-5.012
711.0909	Ni I 64	W	0.295	10.42	-5.297	0.9977	-5.296
711.1453	C I 26	B	0.056	19.22	-5.804	0.9941	-5.799
711.4557	Fe I 267	W	0.072	9.01	-5.979	0.9974	-5.978
711.8099	Fe I 1278	B	0.110	9.56	-5.806	0.9930	-5.802
712.4993	Fe Ip 815	B	0.016	9.01	-6.617	0.9937	-6.614
713.0929	Fe I 1051	B	0.587	13.08	-4.895	0.9871	-4.890
713.2992	Fe I 1002	W	0.370	10.20	-5.233	0.9978	-5.232
714.2524	Fe I 1274	B	0.290	10.99	-5.289	0.9931	-5.287
715.1474	Fe I 109	R	0.206	9.55	-5.509	0.9985	-5.509
715.5636	Fe I 1276	R	0.260	10.73	-5.331	0.9846	-5.324
718.0000	Fe I 33	W	0.176	8.71	-5.626	0.9966	-5.625
718.9156	Fe I 463	R	0.333	9.87	-5.287	0.9938	-5.285
719.0126	Fe I 463	R	0.112	9.43	-5.771	0.9992	-5.771
721.2440	Fe I 1273	R	0.250	10.70	-5.354	0.9957	-5.352
721.9688	Fe I 1001	W	0.399	10.63	-5.192	0.9965	-5.191
722.1206	Fe I 1189	B	0.331	10.98	-5.250	0.9933	-5.247
722.2395	Fe II 73	B	0.153	10.79	-5.602	0.9962	-5.600
722.8699	Fe I 267	B	0.232	9.21	-5.491	0.9940	-5.488
723.5336	Si I 26	B	0.254	13.35	-5.292	0.9894	-5.288
725.1715	Ti I 99	B	0.287	9.58	-5.385	0.9947	-5.384
726.0995	Fe I 267	B	0.155	9.02	-5.682	0.9916	-5.678
726.8562	Fe Ip 957	R	0.062	9.65	-6.040	0.9937	-6.036
728.4838	Fe I 1004	B	0.347	10.62	-5.265	0.9924	-5.262
730.2852	Mn I 50	B	0.096	14.36	-5.705	0.9888	-5.699
730.6570	Fe I 1077	B	0.334	11.12	-5.236	0.9963	-5.234
731.2057	Fe Ip 1310	B	0.050	10.17	-6.128	0.9927	-6.124
732.7651	Ni I 140	R	0.099	10.46	-5.801	0.9977	-5.800
735.5898	Cr I 93	W	0.490	12.07	-5.047	0.9869	-5.042
735.7739	Ti I 97	B	0.186	9.83	-5.570	0.9968	-5.569
738.1941	Ni I 292	B	0.144	11.27	-5.614	0.9955	-5.611
740.0188	Cr I 93	W	0.531	12.81	-4.973	0.9944	-4.971
740.0864	Fe Ip 204	B	0.030	9.96	-6.379	0.9958	-6.377
740.1121	Ni I 291	R	0.110	11.05	-5.721	0.9943	-5.718
740.1689	Fe I 1004	W	0.348	10.52	-5.263	0.9930	-5.260
740.5788	Si I 23	W	0.513	16.58	-4.883	0.9900	-4.878
741.1162	Fe I 1077	R	0.612	14.86	-4.824	0.9889	-4.819
741.8327	Fe Ip 1002	B	0.030	10.10	-6.360	0.9965	-6.358
741.8673	Fe I 1001	R	0.406	11.07	-5.156	0.9981	-5.156
742.1562	Fe I 1188	B	0.143	10.35	-5.663	0.9963	-5.662
742.2285	Ni I 139	R	0.594	13.63	-4.881	0.9924	-4.878
743.0543	Fe I 204	B	0.119	9.02	-5.807	0.9897	-5.802
744.7400	Fe I 1273	B	0.265	11.28	-5.353	0.9955	-5.351
746.1526	Fe I 204	B	0.233	9.80	-5.476	0.9969	-5.475
746.3392	Fe Ip 1307	R	0.069	10.69	-5.950	0.9947	-5.946
746.8284	N I 3	B	0.028	17.11	-6.127	1.0002	-6.128
747.9700	Fe IIp 72	W	0.067	12.38	-5.917	0.9971	-5.915
748.1481	Ni I 286	B	0.079	10.52	-5.920	0.9941	-5.916
748.1744	Fe Ip 266	B	0.041	9.22	-6.268	0.9885	-6.261
748.4305	Fe Ip 1306	R	0.071	10.71	-5.942	0.9954	-5.939
749.1655	Fe I 1077	W	0.485	12.41	-5.031	0.9942	-5.029
749.8535	Fe I 1001	W	0.157	10.13	-5.618	0.9975	-5.616
750.1271	Fe Ip 1002	W	0.029	10.85	-6.339	0.9980	-6.338
750.7271	Fe I 1137	W	0.437	12.12	-5.076	0.9965	-5.075
751.5835	Fe II 73	B	0.111	11.38	-5.726	0.9985	-5.725
752.1041	Ni I 282	R	0.031	13.72	-6.188	0.9967	-6.186
752.2768	Ni I 126	B	0.525	12.78	-4.985	0.9965	-4.983
752.5119	Ni I 139	R	0.506	12.22	-5.011	0.9949	-5.009
753.1153	Fe I 1137	W	0.560	14.09	-4.913	0.9825	-4.905
754.0439	Fe I 266	B	0.098	9.63	-5.856	0.9986	-5.855
754.7897	Fe I 1306	R	0.158	11.72	-5.553	0.9932	-5.550
755.1096	Fe Ip 1303	B	0.080	11.19	-5.888	0.9956	-5.885
755.2486	Ni Ip 286	B	0.070	11.92	-5.915	0.9981	-5.914
755.5605	Ni I 187	B	0.584	14.43	-4.888	0.9946	-4.885
756.8906	Fe I 1077	R	0.517	12.88	-4.977	0.9926	-4.974
757.4048	Ni I 156	W	0.470	12.37	-5.069	0.9863	-5.063
758.2115	Fe Ip 1274	R	0.083	11.97	-5.838	0.9945	-5.835
758.3797	Fe I 402	W	0.573	13.45	-4.945	0.9941	-4.943
761.7992	Fe I 1001	B	0.093	10.25	-5.837	0.9922	-5.832
768.6116	S I 7	B	0.028	15.88	-6.218	0.9986	-6.218
769.8974	K I 1	W	0.832	16.19	-4.706	0.9876	-4.701
771.1727	Fe II 73	R	0.345	12.34	-5.193	0.9944	-5.190
771.5582	Ni I 109	R	0.360	12.38	-5.187	0.9916	-5.183
771.9053	Fe I 1304	R	0.216	11.90	-5.403	0.9968	-5.401
772.3212	Fe I 108	R	0.333	10.18	-5.309	0.9818	-5.302
772.7616	Ni I 156	B	0.569	14.89	-4.902	0.9952	-4.900
773.7668	Fe Ip 1137	R	0.022	12.41	-6.426	0.9965	-6.424
774.5515	Fe I 1305	B	0.163	11.46	-5.563	0.9919	-5.558
775.1114	Fe I 1304	W	0.335	12.44	-5.204	0.9955	-5.202
776.4659	Mn I 54	R	0.028	12.74	-6.308	0.9944	-6.304
777.1959	O I 1	R	0.336	20.51	-4.994	0.9962	-4.992
777.4171	O I 1	R	0.299	20.09	-5.062	0.9951	-5.060
779.7587	Ni I 201	W	0.520	13.54	-4.967	0.9964	-4.965
780.7913	Fe I 1303	W	0.411	13.30	-5.080	0.9984	-5.079
782.0793	Fe Ip 1118	B	0.045	10.20	-6.169	0.9954	-6.166
782.6756	Ni I 109	B	0.087	12.01	-5.828	0.9965	-5.826
784.4552	Fe I 1250	W	0.096	11.26	-5.800	0.9968	-5.798
786.3786	Ni I 268	B	0.105	12.52	-5.720	0.9970	-5.719
791.2384	Si I 68	R	0.073	14.67	-5.809	0.9932	-5.804
794.1095	Fe I 623	R	0.345	11.00	-5.264	0.9983	-5.263
794.9153	Ti I 125	B	0.085	10.60	-5.906	0.9965	-5.905
795.4942	Fe Ip 402	B	0.056	10.14	-6.078	0.9948	-6.075
795.5699	Fe I 1305	R	0.179	12.08	-5.513	0.9954	-5.510
795.9151	Fe I 1304	B	0.166	11.72	-5.559	0.9970	-5.557

TABLE V. — *Number of clean lines per spectral species, in alphabetical order.*

Al I	1	Hf II	1	O I	3	Ti I	75
C I	2	K I	1	Pr II	1	Ti II	2
Ca I	8	La II	3	Ru I	2	V I	25
Ce II	6	Mn I	7	S I	1	V II	2
Co I	25	Mo I	1	Sc I	6	Y I	2
Cr I	61	N I	1	Sc II	8	Y II	3
Cr II	6	Na I	1	Si I	15	Zn I	1
Fe I	358	Nd II	3	Sm II	2	Zr I	3
Fe II	22	Ni I	88	Sr I	1	Zr II	3

TABLE VI.

Wavelength	Mult	log(gf)	Wavelength	Mult	log(gf)	Wavelength	Mult	log(gf)	Wavelength	Mult	log(gf)	Wavelength	Mult	log(gf)
404.191	602	-3.094	525.302	113	-3.906	575.441	866	-2.905	635.384	13	-6.571	697.047	463	-3.845
419.449	274	-3.369	526.262	1149	-2.262	575.926	1184	-2.136	637.619	1140	-3.056	697.194	404	-3.494
428.159	171	-4.121	527.965	584	-3.598	576.034	867	-2.534	638.572	1253	-1.897	698.853	167	-3.529
431.945	214	-3.614	529.454	875	-2.766	576.053	1054	-3.257	639.254	109	-4.039	700.062	1005	-2.247
439.230	757	-2.982	529.531	1146	-1.610	577.846	209	-3.557	641.111	1256	-2.374	700.797	1078	-1.932
441.339	1046	-2.556	530.039	1240	-2.416	578.466	686	-2.678	643.641	1016	-2.465	701.035	1221	-1.985
443.964	515	-3.055	530.131	1162	-2.812	579.392	1086	-1.682	653.394	1197	-1.346	702.407	1003	-2.073
448.597	825	-2.518	530.868	1091	-2.600	580.798	1178	-2.604	659.131	1229	-2.095	706.954	205	-4.358
450.421	988	-3.348	532.003	877	-2.600	580.988	1084	-3.088	660.803	109	-4.026	707.186	1194	-1.497
454.322	893	-3.392	532.681	1147	-2.094	581.191	1022	-2.443	662.503	13	-5.350	707.281	1003	-2.850
454.647	1047	-2.572	535.811	628	-3.267	581.481	1086	-1.904	662.755	1174	-1.586	708.340	1277	-1.398
455.165	972	-2.071	537.683	1132	-2.135	582.787	552	-3.225	666.743	168	-4.435	711.456	267	-4.020
455.693	638	-2.674	538.633	1064	-1.797	583.510	1084	-2.248	666.772	1228	-2.161	711.810	1278	-1.630
456.603	1169	-3.303	539.522	1143	-1.809	583.770	1129	-2.375	669.914	1228	-2.172	712.499	815	-3.724
459.353	971	-2.001	540.127	1146	-1.629	584.492	1056	-3.021	670.357	268	-3.073	713.299	1002	-1.747
460.709	724	-3.588	541.279	1162	-1.872	584.969	922	-3.025	670.449	1052	-2.691	714.252	1274	-1.018
463.078	969	-3.174	542.215	1145	-2.267	585.315	35	-5.173	671.032	34	-4.909	715.147	109	-3.679
465.830	591	-3.005	543.803	1237	-2.692	585.508	1179	-1.654	671.375	1255	-1.497	715.564	1276	-1.022
470.630	890	-3.032	544.340	1059	-2.974	585.609	1128	-1.640	672.536	1052	-2.275	718.000	33	-4.802
471.684	634	-3.492	547.009	1144	-1.658	585.878	1084	-2.259	673.316	1195	-1.499	718.916	463	-2.787
472.614	384	-3.234	549.183	1031	-2.300	586.111	1084	-2.425	673.653	1122	-3.144	719.013	463	-3.386
474.513	67	-4.172	549.446	1024	-2.018	587.628	1084	-2.781	673.952	34	-4.923	721.244	1273	-1.117
476.007	384	-3.705	549.959	1159	-2.754	587.949	1201	-2.063	674.597	1005	-2.758	722.121	1189	-1.309
478.081	633	-3.356	552.128	1162	-2.570	588.003	1201	-2.019	675.347	1196	-2.393	722.870	267	-3.380
478.749	408	-4.245	552.424	1059	-2.902	588.128	1178	-1.840	675.655	1120	-2.826	726.100	267	-3.644
479.056	1068	-2.531	553.928	871	-2.647	590.247	1234	-1.927	678.686	1052	-1.988	726.856	957	-2.941
479.075	632	-3.339	554.699	1061	-1.904	593.381	1198	-2.205	679.326	1005	-2.487	728.484	1004	-1.725
479.397	512	-3.560	555.269	1281	-1.835	594.753	1199	-2.108	679.612	1007	-2.461	730.657	1077	-1.637
479.436	115	-3.965	556.886	869	-2.979	596.957	1086	-2.778	680.187	34	-5.876	731.206	1310	-1.956
479.907	1098	-2.813	557.702	1314	-1.552	597.617	1125	-3.222	680.428	1225	-1.916	734.850	1004	-2.870
480.253	1206	-1.775	558.757	1026	-1.765	601.524	63	-4.741	680.685	268	-3.210	740.086	204	-4.513
480.815	633	-2.696	559.505	1314	-1.842	601.937	780	-3.300	682.037	1197	-1.215	740.169	1004	-1.669
480.994	793	-2.621	560.898	1108	-2.376	603.404	1142	-2.455	682.485	1280	-2.232	741.833	1002	-3.030
490.861	115	-4.195	560.997	866	-3.250	605.408	1142	-2.331	683.324	1194	-2.033	742.156	1188	-1.805
495.430	1093	-3.193	561.136	869	-2.997	608.957	1327	-.922	683.701	1225	-1.789	743.054	204	-3.917
496.192	845	-2.417	561.960	1161	-1.546	609.365	1177	-1.451	683.983	205	-3.424	744.740	1273	-1.104
498.762	1094	-2.940	563.582	1088	-1.654	609.438	1177	-1.652	685.164	34	-5.388	746.153	204	-3.549
499.279	1110	-2.323	563.670	868	-2.602	609.709	64	-5.082	685.572	1194	-1.789	746.339	1307	-1.734
499.541	1113	-2.164	564.436	1057	-3.255	609.825	1200	-1.897	685.725	1006	-2.154	748.174	266	-4.247
501.648	1089	-1.669	565.147	1161	-1.869	612.026	14	-5.940	686.010	1255	-2.431	748.431	1306	-1.706
504.712	1242	-2.443	565.232	1108	-1.836	615.741	624	-3.865	686.194	109	-3.844	749.854	1001	-2.220
505.849	884	-2.823	566.102	1234	-2.484	615.938	1175	-1.948	686.250	1191	-1.496	750.127	1002	-2.962
511.991	960	-3.031	566.134	1108	-1.889	618.740	342	-4.193	686.431	1186	-2.338	754.044	266	-3.840
514.573	931	-3.095	567.769	1057	-2.705	619.951	208	-4.412	688.063	1051	-2.372	754.790	1306	-1.235
515.995	1095	-2.678	567.839	982	-3.040	622.078	958	-2.447	689.829	1078	-2.209	755.110	1303	-1.646
520.529	1112	-3.056	568.024	1026	-2.367	622.674	981	-2.154	693.063	1221	-2.080	758.212	1274	-1.710
520.681	1095	-2.551	570.726	866	-3.588	629.055	208	-4.438	693.362	167	-3.537	761.799	1001	-2.419
521.380	962	-2.819	573.823	1084	-2.297	630.347	1140	-2.671	693.362	1005	-1.903	771.905	1304	-1.095
522.318	880	-2.344	574.185	1086	-1.727	631.151	342	-3.206	693.650	1196	-2.273	772.321	108	-3.556
523.824	962	-3.133	574.296	1084	-2.421	633.085	1254	-1.287	696.032	1222	-2.014	773.767	1137	-2.841

Wavelength	Mult	log(gf)
774.552	1305	-1.261
775.111	1304	-.793
782.079	1118	-2.686
784.455	1250	-1.776
794.110	623	-2.525
795.494	402	-3.824
795.570	1305	-1.239
795.915	1304	-1.301

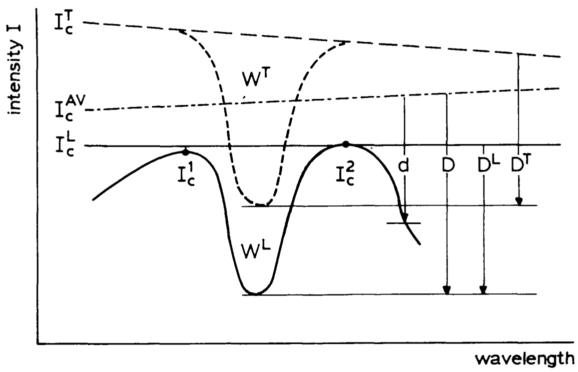

FIGURE 1. — Definition of line parameters. A quasi-continuous « line haze » of unresolved blends lowers the « true » continuum I_c^T to the observed « local » continuum I_c^L. The observed line (solid curve between the maxima I_c^1 and I_c^2) has a local equivalent width W^L ; the dashed profile with equivalent width W^T is the true line, *i.e.* the line one would observe if the blends were not present. The dot-dashed line is the extended Ardeberg-Virdefors continuum I_c^{AV} defined in section 2.2. The depth d is measured from the latter continuum ; $d = 1$ for $I = 0$, and $d = D$ at the minimum of the observed line. D^L and D^T are the local and true fractional depths of the line, respectively. Intensities are measured in arbitrary units, wavelengths and equivalent widths in nm (1 nm = 10 Å).

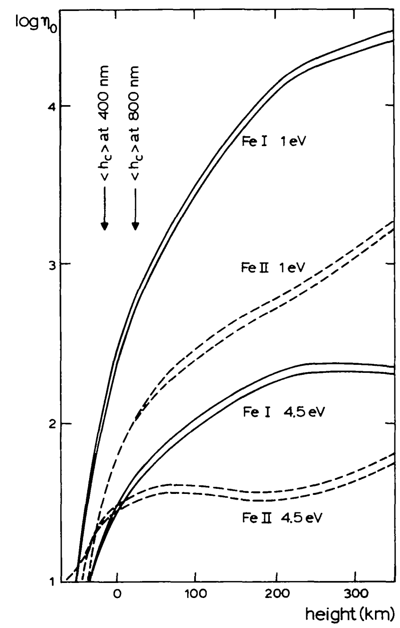

FIGURE 3. — The logarithm of the ratio of the line and continuum absorption coefficients $\eta_0 = l_0/k_c$ at line center, against the height in the photosphere. The arrows mark the mean heights of formation of the continuum at $\lambda = 400$ nm and $\lambda = 800$ nm. The upper curve of each pair is for $\lambda = 800$ nm, the lower for $\lambda = 400$ nm. Each pair of curves has been shifted vertically by an arbitrary amount.

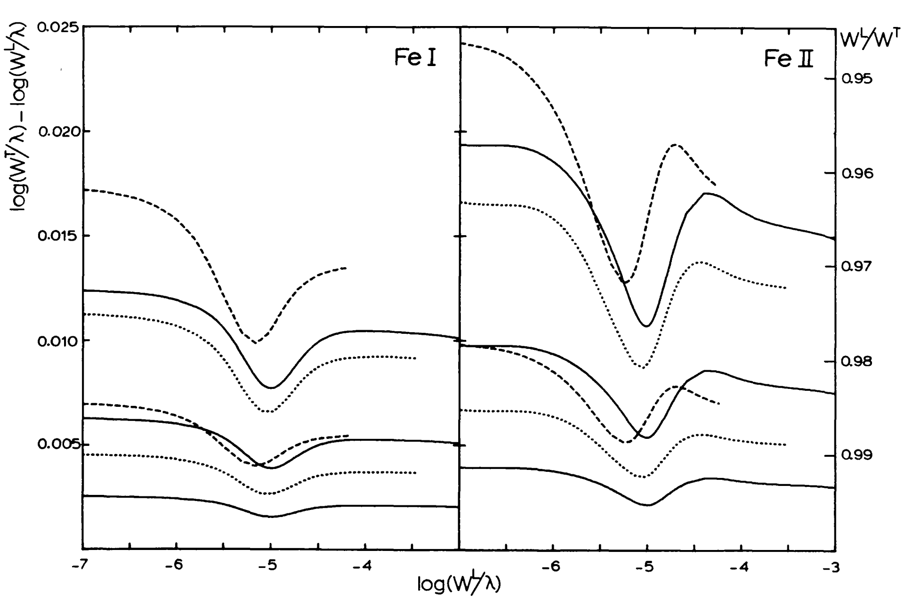

FIGURE 2. — Line-strength correction curves for Fe I lines (left) and Fe II lines (right), respectively at $\lambda = 400$ nm and $\chi = 1$ eV (solid), $\lambda = 500$ nm and $\chi = 3$ eV (dotted) and at $\lambda = 800$ nm and $\chi = 4.5$ eV (dashed). W^T is the true equivalent width computed without opacity enhancement ; W^L is the local equivalent width of the same line but computed with increases of the continuous opacity by $\varepsilon = 2$ %, 5 % and ($\lambda = 400$ nm only) 10 %.

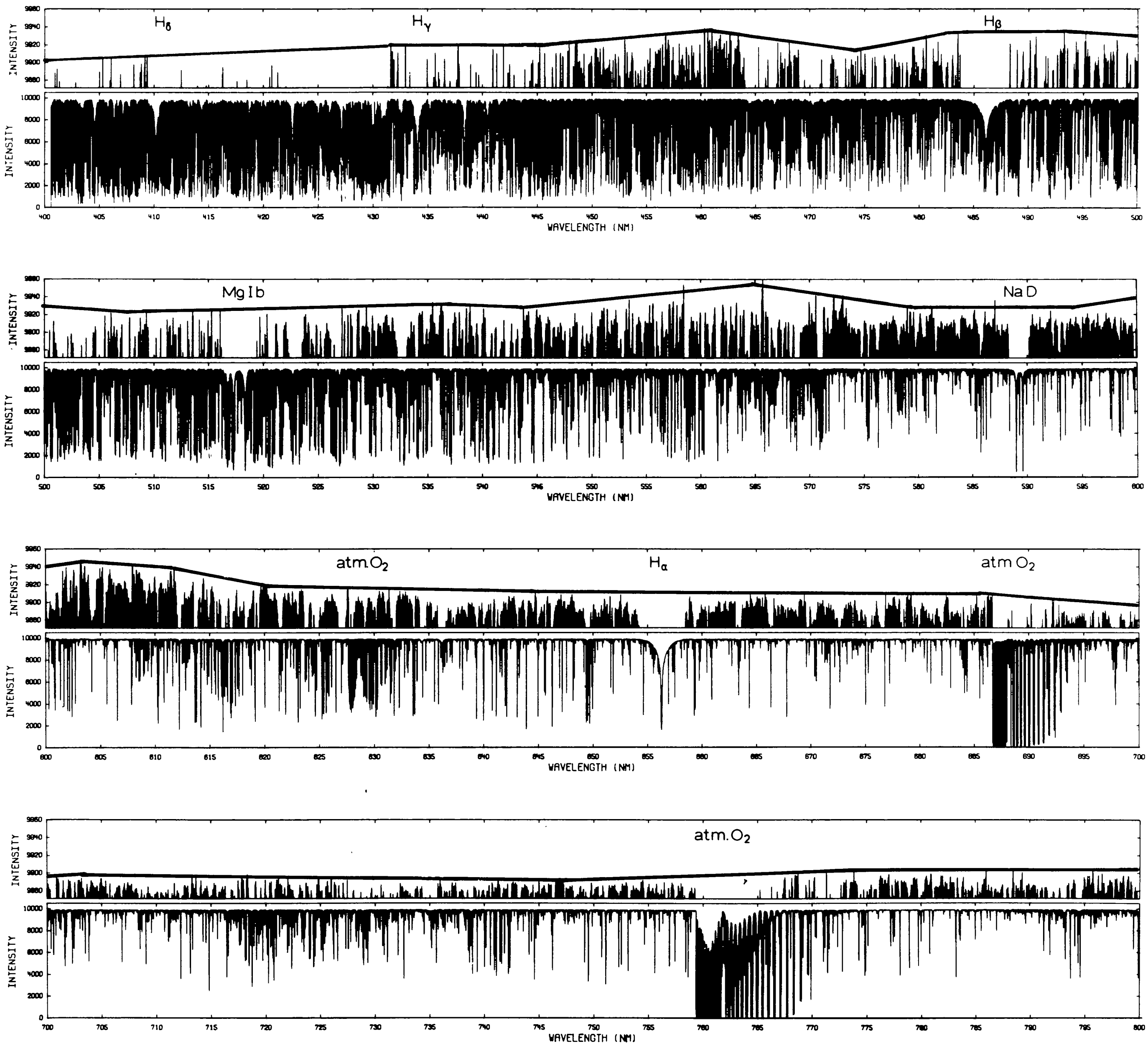

FIGURE 4. — Low-dispersion high-resolution plot of the Jüngfraujoch Atlas of the solar spectrum $\lambda\lambda$400.6-800 nm. The bottom panel of each wavelength strip shows the disk-center intensity in tape-edition units (0-10000). The top panel of each strip shows the top 0.8 % (9870-9960) only, to emphasize the continuum windows. The $I = 100$ level of the graphical edition is at 10000 ; it exceeds the highest windows. The solid line in the continuum panels is the extended Ardeberg-Virdefors continuum I_c^{AV}. Sampling resolution : 1 pm (every fifth tape-edition value).

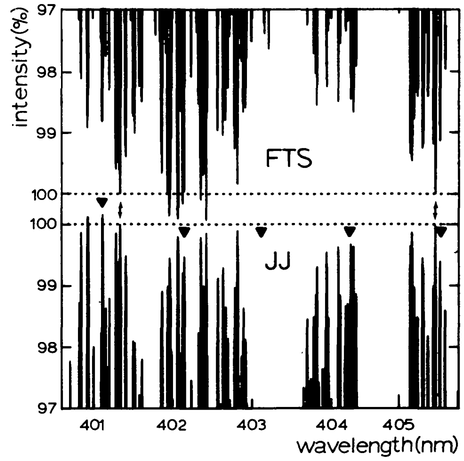

FIGURE 5. — Comparison of the Jungfraujoch Atlas with KPNO FTS data for the region of overlap. The continuum windows of the Atlas are shown on an exaggerated scale at the bottom; the corresponding windows in the FTS data are on top, on a reversed intensity scale. Each data set is normalized to a straight line (dotted) connecting the $\lambda = 401.34$ nm and $\lambda = 405.31$ nm peaks (arrows), which are the highest peaks in the unnormalized FTS data and in the Atlas data, respectively. The triangles mark the endpoints of adjacent Atlas segments. Sampling resolutions : 0.2 pm for the Atlas, 0.5 pm for the FTS data.

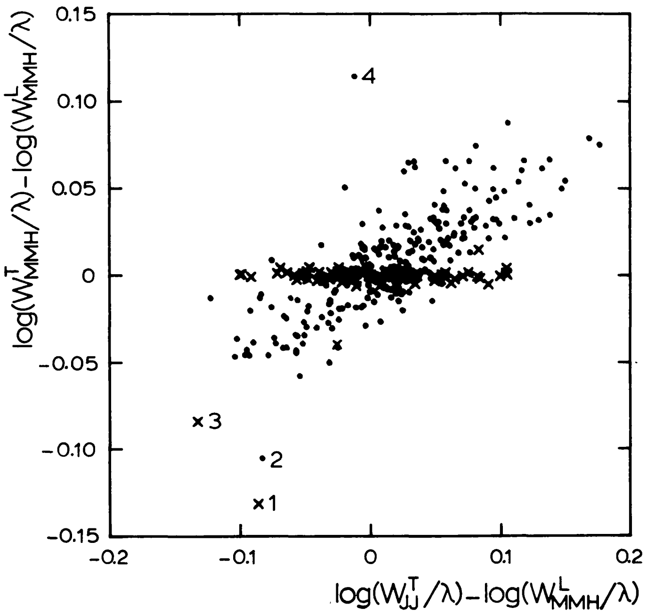

FIGURE 7. — The MMH corrections against the difference between the corrected Jungfraujoch line strengths and the uncorrected MMH line strengths, for the stronger lines only. Dots : lines for which MMH have averaged their equivalent-width measurement with values from the literature (printed in italics in MMH). The numbers identify deviating lines : 1 = λ653.394, 2 = λ554.699, 3 = λ588.382, 4 = λ649.895.

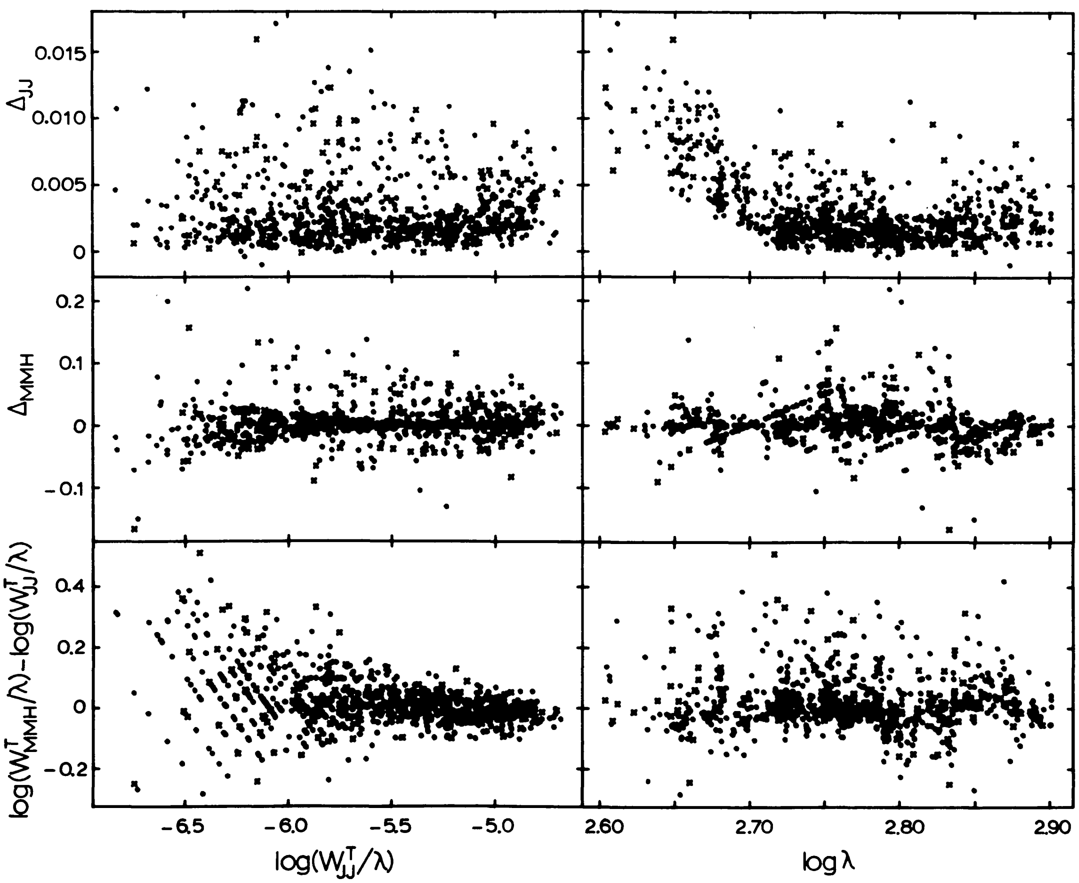

FIGURE 6. — Scatter diagrams for the 750 clean lines. Abscissae : corrected line strength log (W^T_{JJ}/λ) from the Jungfraujoch Atlas (left); logarithm of the wavelength in nm (right). The top panels show the background corrections for the Jungfraujoch Atlas; the middle panels show the MMH corrections; the bottom panels show the differences between the corrected MMH and Jungfraujoch line strengths. Dots : half profile

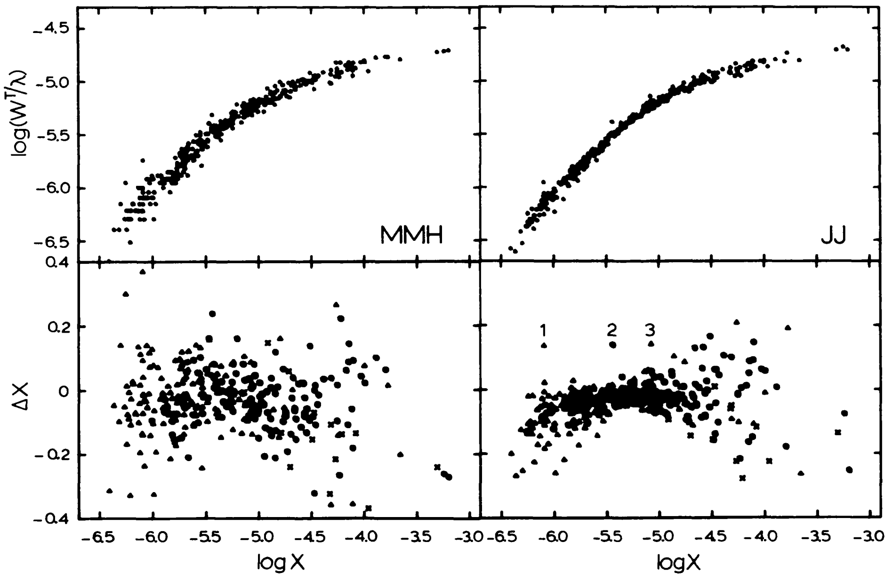

FIGURE 8. — Results for 316 clean Fe I lines. Top panels : NLTE curves of growth, respectively with line strengths from MMH (left) and from the Jungfraujoch Atlas (right). Bottom panels : horizontal deviations of the individual points of each curve of growth from the $\lambda = 550$ nm standard curve of growth of paper RZ. Crosses : Oxford lines; triangles : non-suspect Kiev lines with $\log gf < -2.0$; circles : suspect Kiev lines with $\log gf > -2.0$. The numbers identify three deviating lines, respectively : 1 = λ514.573, 2 = λ707.186, 3 = λ467.284.

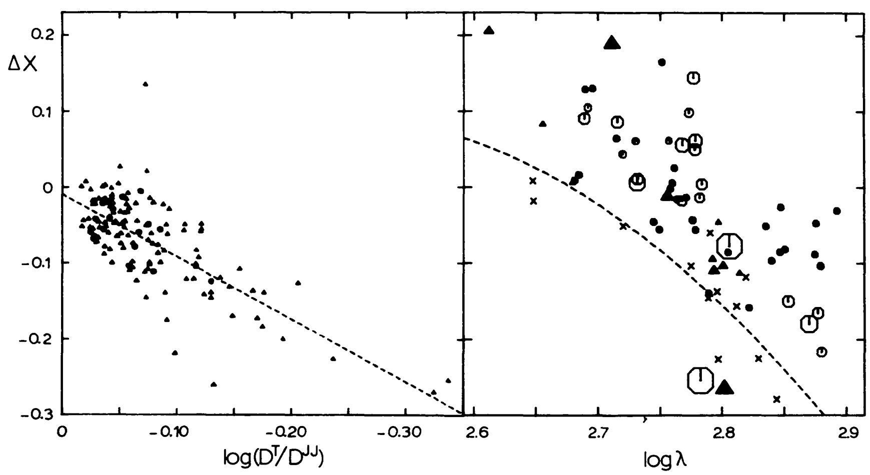

FIGURE 9. — Ordinate : horizontal deviations as in the lower-right panel of figure 8. Left : against $\log (D^{T}/D^{JJ})$, for the weak Fe I lines ($\log X < -5.5$) only. Right : against the logarithm of the wavelength in nm, for the strong lines ($\log X > -4.8$) only. Symbol coding as in figure 8 ; the size of the symbols in the righthand panel increases with the product of the line strength and the differential mean square radius taken from Warner (1969).

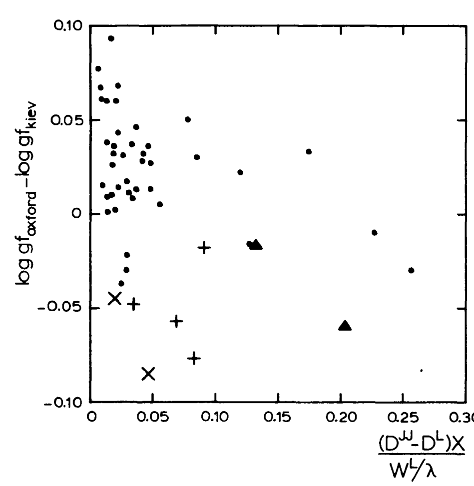

FIGURE 10. — Comparison of Kiev and Oxford gf-values for the lines of overlap. The abscissa measures the effect of the Kiev background error on the Kiev oscillator strengths for the strongest lines. Crosses : weak lines with the background error; plusses : blended lines ; triangles : lines with the NLTE error.